Marina Rodrigues Jorge

Experimental measurement of the electroluminescence yield of pure xenon and mixtures of xenon with percentage quantities of CH$_4$

· U C ·

UNIVERSIDADE DE COIMBRA

To my parents

Acknowledgements

To Luís Manuel Panchorrinha Fernandes and Cristina Maria Bernardes Monteiro for the supervision of the present work and for all the support, suggestions and fruitful discussions along these two years.

To Professor Joaquim Marques Ferreira dos Santos for all the support, suggestions and fruitful discussions. And also for inviting me to GIAN in 2012, to follow Elisabete's work and learn how complex investigation is.

To Elisabete Dinora Caldas de Freitas for introducing me to the experimental system used in this work, for the many suggestions, advice, patience, kindness, constant monitoring in a very supporting sort of way and also for teaching me how to start the investigation process and how to think differently. Elisabete Freitas was there most of the time, alerting me if I made mistakes and explaining me ways to solve them. She was a good co-worker, teacher and friend. I am indebted to her.

To all the members of GIAN that I had the chance to meet, and to Fernando for showing me around twenty scientific articles about the theme of my dissertation and also for the advice. To Paulo Gomes for all the informatic support throughout the last two years.

To José Paulo Domingues for the clarifications about dissertation deadline and other topics on that matter.

To Carlos Alberto Henriques, for being a good co-worker and friend, a master student that shared his difficulties and for giving me plenty important advice.

To all my friends in GIA: Xavier Carvalho, Daniel Mano and Emanuel Barata.

To my friends João Abílio Almeida and Pedro Borlido for inviting me to lunch every day in the last months, when we spent all day writing our dissertations.

To Alice de Castro, Andreia Domingues, Elsa Gonçalves and Mariana David for long years of the great friendships. And also to Dolly Alberto, João Domingues, Joel Oliveira, Juliana Gomes and Marta Henriques for being also such good friends, giving me support and for the happy time we spent together.

To my friend Bruno Agatão for answering some English grammatical questions and for joining me to run after a day's of work, and also for being a good friend since the day we met.

To all of those who, in any possible way, contributed to the fulfilment of this work.

To my parents who always supported most of my decisions and made many sacrifices for letting me study at the University. I was grateful for the food, the advices, and the concern and for giving me strength.

To my brother Pedro Jorge for all the support and friendship since I can remember.

To my goddaughter Ana Júlia Rodrigues for the long years of friendship, understanding and everything else.

And also to my uncles, aunts, cousins, grandmother and grandfather for being so kind.

List of Abbreviations

EL – Electroluminescence

GPSC – Gas proportional scintillation counter

NEXT – Neutrino experiment xenon TPC

TPC – Time projection chamber

HPGXe – High-pressure xenon gas

R&D – Research and development

GIAN - Atomic and Nuclear Instrumentation Group

GPSC - Gas Proportional Scintillation Counter

$\beta\beta0\nu$ - Neutrinoless double beta decay

$\beta\beta2\nu$ – Double beta decay with emission of two neutrinos (standard two neutrino mode)

$\beta\beta$ - Double beta decay

ER – Energy resolution

Z – Atomic number

VUV – Vacuum Ultraviolet

FWHM - Full width half maximum

SOFT - Separated optimized function

PMT – Photomultiplier tube

APD - Avalanche Photodiode

Abstract

Electroluminescence (EL), as signal amplification method of primary ionisation of noble gases in Gas Proportional Scintillation Counters (GPSC), developed in the 1970's, has played an important role in applications to many fields such as astronomy, plasma physics and high-energy physics, up to rising of solid state detectors in the mid 1990's. However, in the last years EL amplification recovered importance in experiments for rare event detection, such as direct dark matter and double beta decay searches.

The Neutrino Experiment with a xenon TPC, NEXT, is an international collaboration that aims at measure the neutrinoless double beta decay, $0\nu\beta\beta$, of the isotope ^{136}Xe.

Recent Monte Carlo simulation studies performed in Coimbra pointed out different trends for several gases added to xenon. While the presence of CH_4 in levels of the order of the percent or below does not have important impact on the EL reduction, the addition of CF_4 reduces significantly the EL, even for amounts of few decimals percent. A compromise must be found between the reduction of EL and the amount of molecular additive.

It is of great importance for the NEXT Collaboration to have these R&D studies performed, both experimentally and by simulation. The Atomic and Nuclear Instrumentation Group (GIAN) of the Instrumentation Centre at the University of Coimbra, has large expertise in the field, assuming the responsibility to carry out the detailed studies on this topic.

In the present work, relative measurements have been performed for the EL yields of xenon and xenon-mixtures in a uniform electric field driftless GPSC. The operational parameters of the detector, including amplitude, energy resolution and drift velocity, were measured as a function of the reduced electric field in the scintillation region. The results obtained agree with those from Monte Carlo simulations.

Resumo

A Eletroluminescência (EL), como método de amplificação de sinal da ionização primária produzida em gases nobres, em contadores gasosos de cintilação proporcional (CGCP), desenvolvidos na década de 1970, tem desempenhado um papel importante em aplicações a diversas áreas, tais como astronomia, física dos plasmas e física das altas energias, até meados dos anos 1990 com a evolução dos detetores de estado sólido. No entanto, nos últimos anos a EL recuperou importância em experiências para a deteção de eventos raros, como a procura de matéria negra e do decaimento beta duplo.

NEXT *(Neutrino Experiment in a xenon TPC)* é uma colaboração internacional que tem como objetivo medir o decaimento beta duplo sem emissão de neutrinos, $0\nu\beta\beta$, no isótopo ^{136}Xe.

Estudos recentes de simulação Monte Carlo realizados em Coimbra apontam tendências diferentes para cada gás adicionado ao xénon. Enquanto a presença de CH_4 em quantidades da ordem de um por cento ou inferior não tem impacto importante na redução de EL, a adição de CF_4 reduz significativamente a EL, mesmo em quantidades de algumas décimas percentuais. Um compromisso deve ser encontrado entre a redução de EL e a quantidade de impurezas moleculares a adicionar ao xénon.

É de grande importância para a colaboração *NEXT* que estes estudos de I&D sejam realizados, tanto experimentalmente como por simulação. O Grupo de Instrumentação Atómica e Nuclear (GIAN) do Centro de Instrumentação da Universidade de Coimbra tem grande experiência na área, tendo ficado a seu cargo a realização de estudos detalhados sobre este tema.

No presente trabalho, foram realizadas medidas relativas do rendimento de EL em xénon e em misturas de xénon usando um CGCP sem região de deriva com um campo elétrico uniforme. Outros parâmetros investigados, incluindo a amplitude, resolução em energia e velocidade de deriva, foram medidos em função do campo elétrico reduzido na região de cintilação. Os resultados obtidos são concordantes com os resultados de simulação de Monte Carlo.

Contents

1. NEXT and Neutrinoless Double Beta Decay

The Neutrino Experiment in a xenon TPC, NEXT, is an international collaboration that aims to measure/search the neutrinoless double beta decay, $0\nu\beta\beta$, in xenon-136 at the *Laboratorio Subterráneo de Canfranc* (LSC) in Spain. NEXT has the collaboration of 14 different institutions and around 80 investigators to carry out the conception, development and construction of a 100 kg high pressure xenon gas (HPGXe) Time Projection Chamber (TPC) to be able to perform the experiment [1].

Double beta decay ($\beta\beta$) is a nuclear transition in which the nucleus maintains its mass number but increases its atomic number from Z to Z+2. It can only occur if the decay to Z+1 atomic number is forbidden energetically. All double beta decay experiments have to deal with an intrinsic background, the $\beta\beta2\nu$, which can only be suppressed by good energy resolution. To suppress cosmic background the detector is operated in an underground laboratory. Natural radioactivity from the detector materials and environmental elements can easily overwhelm the signal and, therefore, the use of radio-pure materials is of huge importance. Additional experimental choices and procedures that increase the separation of signal from background are welcome and render the result more robust.

Xenon is a slow gas, having very large electron diffusion. These characteristics are a drawback for the pattern recognition needed for the TPC. The addition, in small quantities, of a molecular gas such as CH_4 or CF_4 can have a great impact on the reduction of diffusion and on the increase of the drift velocity.

However, drifting electrons may undergo $\sim 10^4$ elastic collisions before gaining from the electric field enough energy to excite the xenon atoms and produce electroluminescence (EL). If a collision occurs between an electron and a polyatomic molecule, the electron energy may be lost without resulting in EL, if the electron transfers its energy to the molecule through vibrational and rotational excitation; this process reduces the EL drastically. A compromise must be found between the reduction of EL and the amount of molecular additive.

Recent Monte Carlo simulation studies performed in Coimbra [2,3,4] pointed out different trends for each gas; while the presence of CH_4 of the order of the percent or below does not have important impact on the EL reduction, the addition of CF_4 reduces the EL significantly, even for amounts of few tenths of percent.

It is, therefore, of great importance for the NEXT Collaboration to have these R&D studies performed, both experimentally and by simulation. Because our research group has large expertise in the field, it was up to our group, the Atomic and Nuclear Instrumentation

Group, GIAN, of the Instrumentation Centre, University of Coimbra, to carry out the detailed studies on this topic.

The objectives of the work described in this thesis were at first the assembly of a driftless GPSC, i.e. a detector without drift region. It was equipped with two gas systems, one for purification and circulation of the gas and another, independent of the former, for addition of molecular impurities.

Since the drift region is not present and the electric field in the scintillation region is high, the effect of electron attachment during the drift of the electrons through the small thickness of the scintillation region is negligible; only the effect of the loss in scintillation yield will be measured. As the X-ray absorption is shallow, a few mm, compared to the scintillation region thickness, of a few cm, the different penetration depths of the X-rays in the scintillation region present only a small effect that can be corrected for. Further on, as the ultimate objective, studies were performed for the scintillation yield as a function of reduced electric field in the scintillation region, for xenon only and for doped xenon, adding molecular concentrations between 0.5 to 2% of CH_4 at pressures of about 1 bar.

1.1 Double Beta Decay

Double beta decay (ββ) is a nuclear transition in which the nucleus maintains its mass number but increases its atomic number from Z to Z+2. It can only occur if the decay to Z+1 atomic number is forbidden energetically. There are two modes of ββ, one with and another without the emission of neutrinos.

The standard two-neutrino mode (ββ2ν) consists in the conversion of two neutrons into protons with the emission of two electrons (e^-) and two electron antineutrino ($\bar{\nu}_e$). This mode is observed in isotopes with years as half-lives of 10^{18}-10^{21} years. Its decay scheme is [1]:

$$_Z^A X \rightarrow\ _{Z+2}^A Y + 2e^- + 2\overline{\nu_e} \qquad\qquad 1.1$$

Neutrinoless double beta decay (ββ0ν) is a hypothetical nuclear transition in which two neutrons experience beta decay simultaneously and without the emission of neutrinos. Its scheme is [1]:

$$_Z^A X \rightarrow\ _{Z+2}^A Y + 2e^- \qquad\qquad 1.2$$

In the ββ0ν decay the two electrons produced have both the same energy, corresponding to half the mass between the parent and daughter nuclei.

The topological signature of ββ0ν decay is a two-electron track with a strong energy deposition at each end, the so-called "blobs".

The ββ0ν search is the most efficient way to reveal if neutrinos are Dirac or Majorana particles.

1.2 Neutrinos and the Standard Model of particle physics

Neutrinos are fundamental and neutral particles with spin ½. They are not influenced either by the strong interaction or by the electromagnetic force. However, they are observed via the weak interaction, whose small strength makes neutrinos very difficult to detect [5].

For more than 30 years the Standard Model has provided the most consistent description of the majority of the phenomena occurring in particle physics. One of the few parts of the Standard Model that does not agree with experimental results is the description of neutrinos, namely where it assumes that neutrinos have zero mass and that neutrinos and antineutrinos are dissimilar particles and that the lepton number is conserved. In fact, (ββ2ν) is fully consistent with the Standard Model of electroweak interaction while (ββ0ν) is totally inconsistent with this model [5].

Recently, neutrino oscillation experiments demonstrated that neutrinos are massive particles [5]. Neutrinoless double beta decay is able to demonstrate the basic nature of neutrinos and can only occur, even so with a very low event rate, if the neutrino is a Majorana particle. The importance of neutrinoless double beta decay emanates from the fact that it necessarily implies a Majorana neutrino mass [6] and, neutrinos being Majorana particles implies that the neutrino is its own antiparticle. The particle emitted as a neutrino by one of the beta decays is absorbed, as an antineutrino, by the other, producing neutrinoless double beta decay (ββ0ν). At last, in (ββ0ν) lepton number conservation is not observed, as in (1.2) and is forbidden by the Standard Model of electroweak interaction and, thus, can only occur if lepton number conservation is not an exact symmetry of nature [7].

1.3 Xenon in neutrinoless double beta decay detection

The isotope xenon-136 was chosen to be used in (ββ0ν) detection because it presents several advantages over other media. Xenon provides both scintillation and ionization signals and, in its gaseous phase, it can provide high energy resolution, better than 0.5% at 2500 keV (Q_{bb} = 2458 keV). It offers the possibility of scaling-up to a large-mass detector, in the ton-scale,

by using high-pressure xenon gas. In addition, the background rate is among the lowest predicted for the new generation of experiments.

Xenon has two naturally-occurring isotopes that can decay by $\beta\beta$, xenon-134 (Q_{bb} = 825 keV) and xenon-136 (Q_{bb} = 2458 keV). Because of its higher Q-value, xenon-136 is preferred over xenon-134 for neutrinoless double beta decay searches, since the decay rate is proportional to $Q^5_{\beta\beta}$ and radioactive background is lower at higher energies.

Xenon-136 constitutes 8.86% of all natural xenon, which implies that the xenon gas has to undergo an enrichment process, although this procedure is relatively simple and non-expensive compared to that of other isotopes; this turns xenon-136 into the most obvious candidate for a future multi-ton experiment. Also, xenon, unlike other $\beta\beta$ sources, doesn't have other long-lived radioactive isotopes that could increase the overall background.

There are several experiments that study double beta decay such as GERDA [8], EXO-200 [9], SNO+ [10], KamLAND-ZEN [11], Lucifer [12], T2K, Exo-gas [13,14] and NEXT [1]. The latter one, in which our research centre takes part, is described in the following section. Among those, the ones using gas target are Exo-gas, SNO+ and NEXT.

1.4 The NEXT Experiment

Neutrino Experiment with a xenon Time Projection Chamber, NEXT, is an international collaboration composed of 14 different institutions from different countries, including the Instrumentation Centre at the University of Coimbra, accounting more than 80 researches in total.

The NEXT experiment was proposed to the Laboratorio Subterráneo de Canfranc (LSC), Spain, in 2009 [5].

NEXT will search for ($\beta\beta0\nu$) in xenon-136 using a high-pressure xenon gas (HPGXe) time projection chamber (TPC).

1.4.1 NEXT-Main objectives and operation principle

The NEXT collaboration has designed and is building a High Pressure Xenon (HPXe) Time Projection Chamber (TPC) with a source mass of 100 kg of xenon at 10 bar, enriched in the isotope xenon-136 for measuring its double-beta decay, both with neutrino and without neutrino emission [1].

Measuring neutrinoless double-beta decay is the main objective of NEXT and the measurement of this phenomenon would establish that neutrinos are Majorana particles (it being their own antiparticles). It would also provide an explanation for the very small neutrino

mass and it will demonstrate that conservation of the total lepton number is violated and, thus, that it is not a conserved quantity in nature, which could be related to the cosmic asymmetry between matter and antimatter in opposition to what is stated in the Standard Model.

1.4.2 The innovative Concept of the experiment

A most important issue for the success of this experiment is the achievable Energy Resolution (ER), which should be better than~1% FWHM (full width half maximum) at $Q_{\beta\beta}$ (2458 keV). It is important because it reduces the tail of $\beta\beta2\nu$ spectrum which overlaps the region of interest of the $\beta\beta0\nu$ spectrum. Another important feature to reduce external background is by identifying the unique signature of $\beta\beta0\nu$ events, a double-electron track, about 30 cm long at 10 bar, tortuous due to multiple scattering, and with larger energy depositions at both ends [1].

1.4.3 Function for Tracking
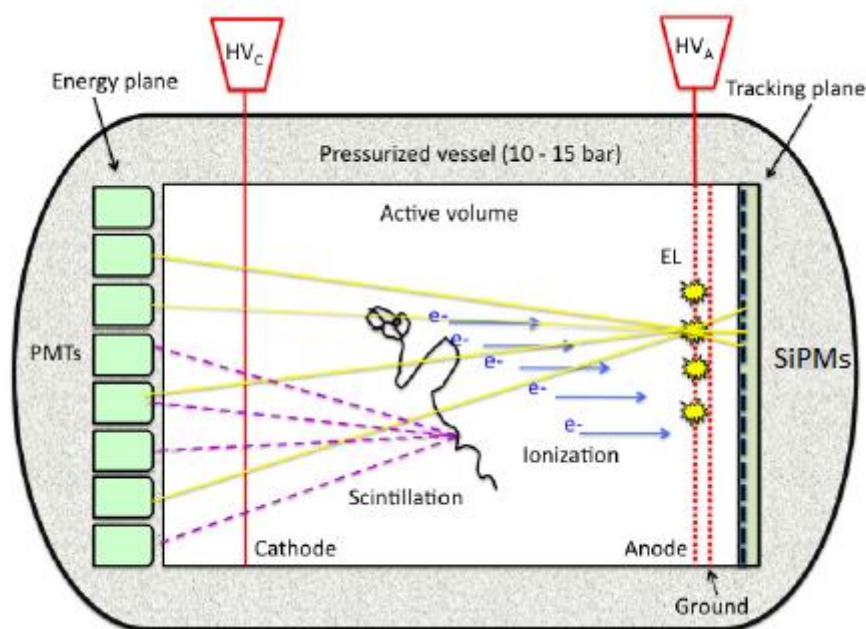
Figure 1.1: The Separate Optimized Functions (SOFT) concept in the NEXT experiment; the PMTs on the left form the energy plane and the SiPMs on the right form the tracking plane [1].

The TPC for NEXT has separate detection systems for tracking and calorimetry. Figure 1.1 represents the detection process based on the separated optimized function (SOFT) concept **[5].** Particles interact in the HPXe gas and transfer their energy to the xenon gas through

ionization and excitation. In the de-excitation processes vacuum ultraviolet (VUV) scintillation light from xenon (~ 178 nm) is emitted.

In the region between the cathode and the anode, the electric field is 0,3 - 0,5 kV/cm to prevent recombination of the positive ions with the free electrons. The ionization electrons drift towards the TPC anode and enter another region where the electric field is of the order of 3 kV/cm/bar. This region with higher electric field is delimited by two highly transparent meshes. In this region, additional EL is produced isotropically.

The pulses from both electroluminescence and ionization are detected in the plane of PMTs located behind the cathode, the so-called energy plane. The start-of-event, t0, is given by the detection of the primary scintillation light, the prompt signal. EL also allows tracking because it is detected, in the anode plane, the tracking plane, placed some millimetres from where the EL production takes place. The tracking plane is composed of 1-mm^2 SiPMs and is important because it will allow to identify, without any doubt, the characteristic track form of the ββ0ν event, namely a tortuous line with the two "blobs", which are due to the high energy deposition at both ends of the track.
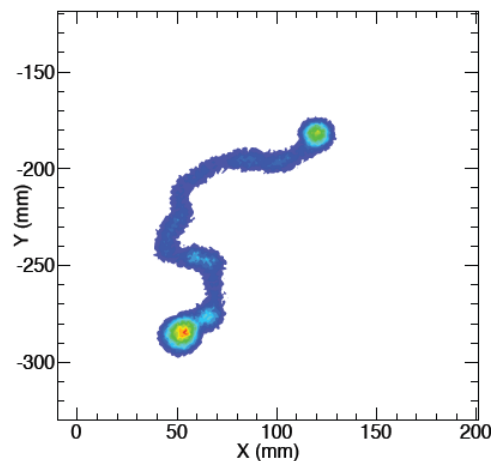
Figure 1.2: Monte Carlo simulation of the charge released in a ββ0ν decay in^{136}Xe gas at 10 bar; the twisted ionization track with 2 "blobs", one on each end of the track, which constitutes the unambiguous signature of a ββ0ν event [1].

1.5 Chapters summary

Chapter 2 presents a description of the electroluminescence processes, the fill gas chosen for the detector and an overview of the design, operation principle and main performance characteristics of a Gas Proportional Scintillation Counter (GPSC).

In chapter 3 the experimental system is presented, namely the GPSC without drift region, the photosensor, the electronic and the gas system. It also has

Chapter 4 presents the experimental results and discussions for the energy resolution, relative amplitude and drift velocity as a function of E/p, its comparison with Monte Carlo simulations from another author and the electroluminescence yield.

Finally, chapter 5 presents the conclusions drawn from this work and ideas that can be developed studied in the future.

1.6 References

[1] V. Álvarez, F.I.G.M. Borges, S. Cárcel et al., NEXT-100 Technical Design Report (TDR). Executive Summary", *JINST* **7** (2012) T06001; doi:10.1088/1748-0221/7/06/T06001

[2] J. Escada, T.H.V.T Dias, P.J.B.M. Rachinhas et al., A study of the electroluminescence yield and fluctuations in xenon doped with CH_4 or CF_4: The role of electron cooling and attachment, Nuclear Science Symposium Conference Record IEEE (2009) 729

[3] J. Escada, T.H.V.T. Dias, F.P. Santos et al., A Monte Carlo study of the fluctuations in xenon electroluminescence yield: pure xenon vs xenon doped with CH_4 or CF_4 and planar vs cylindrical geometries, JINST 6 (2011) P08006

[4] J. Escada, P.J.B.M. Rachinhas, T.H.V.T. Dias et al., Photoelectron Collection efficiency in Xe-CF4 mixtures, Nuclear Science Symposium Conference Record IEEE volume 1 (2007) 585

[5] M. C. G. Garcia and M. Maltoni, Phenomenology with Massive Neutrinos, Physis Reports, 2008.

[6] J. W. F. Valle, Neutrino physics overview, J.Phys.Conf.Ser.53, no. arXiv:hep ph/0608101v1, pp. 473-505, 2006.

[7] A. Faessler and F.Simkovic, Double beta decay, *J.Phys.G24 (1998) 2139-2178*; arXiv:hep-ph/9901215v1.

[8] M. Agostini, M. Allardt, E. Andreotti, et al., Results on neutrinoless double beta decay of ^{76}Ge from GERDA Phase I, *Physical Review Letters*, vol. 111, Article ID 122503, 2013.

[9] M. Auger, D. J. Auty, P. S. Barbeau, et al*.,* Search for neutrinoless double-beta decay in ^{136}Xe with EXO-200, *Physical Review Letters, vol. 109, no. 3, Article ID 032505, 2012*.

[10] C. Kraus and S. J. M. Peeters, The rich neutrino programme of the SNO+ experiment, *Progress in Particle and Nuclear Physics, vol. 64, no. 2, pp. 273–277, 2010*.

[11] A. Gando, Y. Gando, H. Hanakago, et al., Limit on neutrinoless $\beta\beta$ decay of ^{136}Xe from the first phase of KamLAND-Zen and comparison with the positive claim in ^{76}Ge, *Physical Review Letters, vol. 110, no. 6, Article ID 062502, 2013*.

[12] J. W. Beeman, F. Bellini, P. Benetti, et al., Current Status and Future Perspectives of the LUCIFER Experiment, *Advances in High Energy Physics, Volume 2013 (2013), Article ID 237973*; http://dx.doi.org/10.1155/2013/237973

[13] D Sinclair, E Rollin, J Smith, et al., Prospects for Barium Tagging in Gaseous xenon, *Journal of Physics Conference Series 08/2011; 309(1):012005*; DOI: 10.1088/1742-6596/309/1/012005

[14] Kirill Pushkin, Status of the EXO gas detector R&D, http://meetings.aps.org/link/BAPS.2011.APR.Y8.7

2.   Gas Proportional Scintillation Counter

2.1 The Gas Proportional Scintillation Counter

The first detectors used for X-rays fluorescence detection were scintillator detectors and proportional counters. Since these detectors had bad resolution, it was needed to find solutions to improve the energy resolution.

In 1967 Conde and Policarpo developed the gas proportional scintillator counter, with better energy resolution, higher count rate capability operating without space charge effects and higher detection areas when compared with proportional counters [1,2].

2.1.1   General Description

The gas proportional scintillation counter is a radiation detector based on electroluminescence as a signal amplification technique, with the particularity of operating at room temperature.

This detector is usually filled with a high-purity noble gas, typically xenon [2] but argon [3] is also used or noble gas mixtures like Ar+Xe [4], Xe+Kr [5], Ne+Xe [6], or Xe+N_2[2], or even noble gases with molecular impurities, like CH_4, CF_4, CO_2.

The filling pressure is around 1 atmosphere or higher.

The output signal is proportional to the absorbed radiation in the detector. That is why GPSC has 'proportional' in its designation.

2.1.2   Absorption of X-Rays in xenon

When an ionizing radiation is absorbed in the gas, two processes can occur, namely ionization of atoms producing a cloud of primary electrons and excitation of atoms resulting in light known as primary scintillation.

The interaction between X-ray photons and gas atoms can happen through different effects, the photoelectric effect and the Compton effect which are the two more probable, but also Rayleigh scattering and pair production [7].

The main electromagnetic interaction types with matter for energies below 1.02 MeV are photoelectric effect (absorption), Rayleigh effect and Compton Effect, the last two due to photon diffusion.

The photoelectric effect consists in the absorption of an incident photon by an atomic electron and, consequently, its ejection from the atom. The ejected photoelectron has an energy given by the difference between the incident photon energy and the electron binding energy of the occupied layer. This interaction originates an excited ion with a gap in the layer previously occupied by the electron, except when the ionization occurs in the most outer layer of the atom [7].

The probability of X-ray photon absorption depends on the absorption cross section, which is approximately equal to the photoelectric cross section, σ_P.

$$\sigma_P \; \alpha \; \frac{Z^m}{E^{3.5}}$$

2.1

where *Z* is the atomic number of the gas atoms, *m* is a number between 4 and 5 and *E* is the energy of the incident photon. From (2.1), the heavier the noble gas atoms, the stronger the absorption. That is why pure xenon (Z=54) or mixtures with xenon are often used as the filling gases in X-rays detectors.

The Compton effect is the elastic collision between a photon and a free electron at rest. With this collision the photon diffusion through the electron occurs and part of the photon energy is then transferred to the electron. As a result, the incident photon is deflected with an energy depending on the diffusion angle and an energetic electron is emitted.

Rayleigh scattering is an elastic diffusion process of a photon incident on an atom. The photon does not lose almost any energy since the atom has a very large mass. The atom is neither ionized nor excited; only the direction of the incident photon whose energy is preserved, changes.
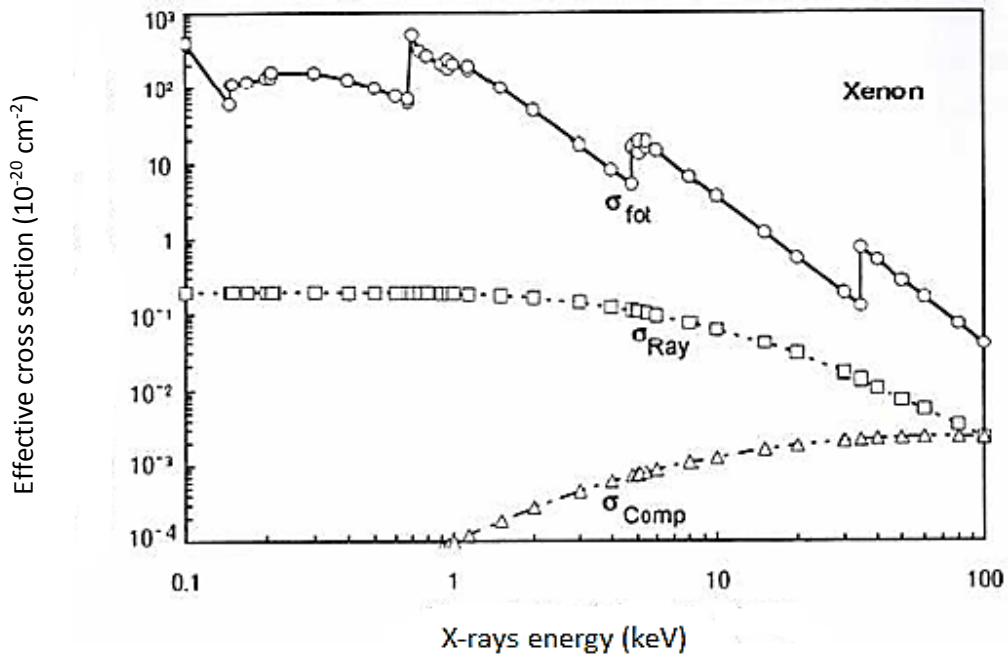
Figure 2.1: Total effective cross section of the photoelectric effect (σ_{fot}), Rayleigh dispersion (σ_{Ray}) and Compton effect (σ_{Comp}) for pure xenon as a function of X-ray energy between 100 eV and 100 keV [8].

For the range of energies considered in figure 2.1, the total effective absorption cross section is higher for the photoelectric effect, so that contributions from other effects are negligible, meaning that, the probability for occurrence of the photoelectric effect is the highest.

As we can see in figure 2.2, photoelectric effect is dominant for photon energies up to 400 keV.
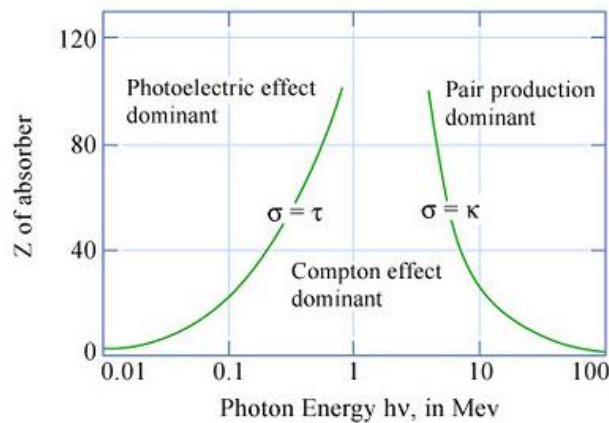
Figure 2.2: Relative importance of the interaction processes between gamma rays and matter [7]

2.1.3 Structure and operation principle

This GPSC is generally composed of three parts, the absorption/drift region, the scintillation region and the photosensor, as represented schematically in figure 2.3.
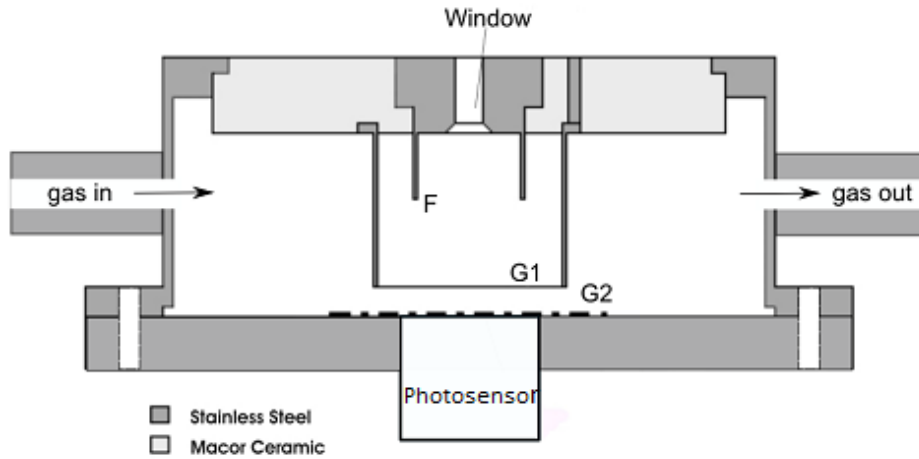
Figure 2.3: Schematic representation of a GPSC

A Macor ceramic is often used between the detector body and the radiation window holder for electrical insulation. Both window and Macor are glued to the stainless steel detector body. The fill gas circulates in a closed circuit that includes elements to purify the gas which is inside the detector.
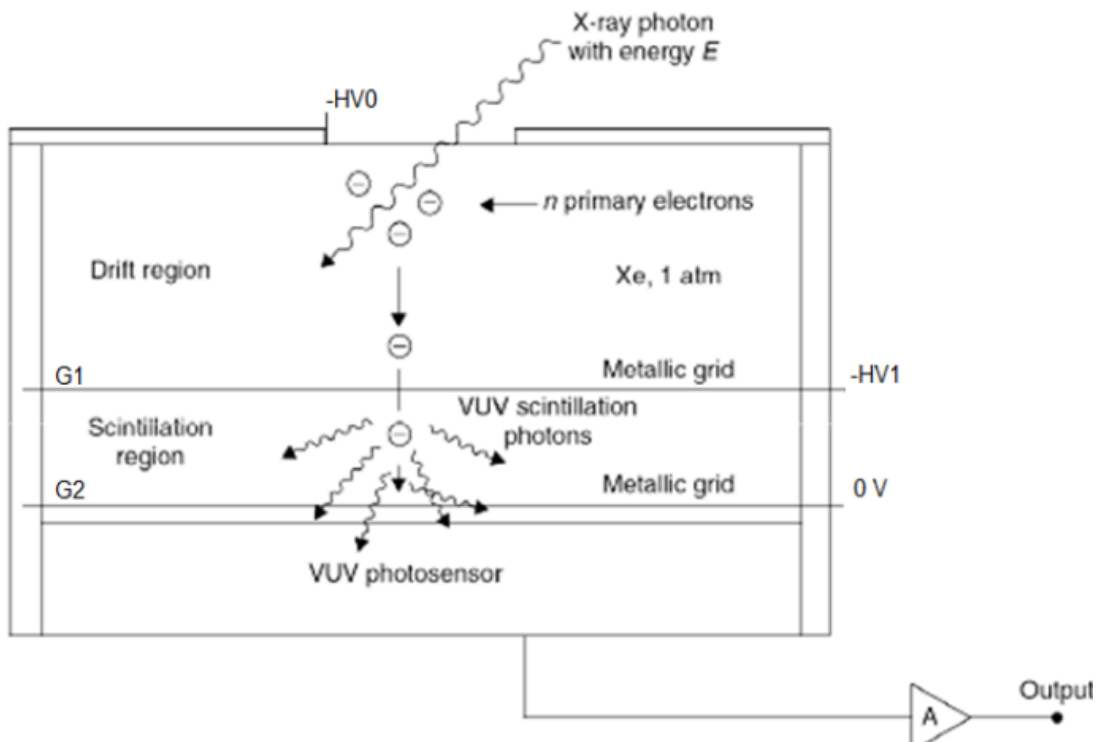
Figure 2.4: Schematic of a GPSC showing the formation of the signal after an X-ray interaction in the gas.

Figure 2.4 shows the different regions of a GPSC and the physical processes taking place in each of them.

2.1.3.1 Absorption/Drift region

The absorption (or drift) region is defined by the radiation detector window and grid G1. The window voltage is -HV0 and lower than the voltage of G1, -HV1, so that the electric field direction points to the window and electrons move in the opposite direction, to the photosensor.

The incident ionizing radiation passes through the radiation window and is mainly absorbed in the gas volume inside the drift region.

As the incident x-ray beam interacts with the gas atoms, a primary electron cloud is produced. The primary scintillation is the result of gas radiative excitation and subsequent de-excitation as well as electron-ion recombination and its intensity is 20% of the total absorbed energy [9,10].So, in general it is not high enough to be detected.

In the drift region, the electric field is weak, smaller than the gas excitation threshold, which in the case of xenon is around 1V/cm/torr. This weak electric field guides the free electron cloud towards the scintillation region, where they undergo elastic collisions with the gas atoms, because the energy gained by the electrons from the electric field is not enough to excite the gas atoms.

2.1.3.2 Scintillation Region

The scintillation region is defined by grids G1 and G2. G2 is at ground.

In this region, a scintillation reduced electric field (E/p) is applied, that is higher than the gas excitation threshold (1V/cm/torr for xenon) but lower than the gas ionization threshold (for xenon 6V/cm/torr). Therefore, while the primary electrons are crossing this region, they acquire enough kinetic energy from the electric field to excite noble gas atoms; when the latter return to the ground state – deexcitacion – they emit vacuum ultraviolet (VUV) photons. This process is called secondary scintillation or electroluminescence (EL).

2.1.3.3 Photosensor

The secondary scintillation produced in the scintillation region of a GPSC filled with a noble gas must be detected with a photosensor sensitive to the wavelength of the light produced inside the detector. For xenon and other noble gases, the photosensor must be

sensitive to VUV light, because the secondary scintillation emission spectra of rare gases centre in this region of the electromagnetic spectrum.

A fraction of the VUV photons is converted in an electric pulse by this VUV sensor. Normally, a Photomultiplier Tube (PMT) or an Avalanche Photodiode (APD) is used.

2.2 GPSC performance

2.2.1 Response Linearity

The interaction of X-rays with energy E_0 in the detector results in the production of primary electrons. In a good approximation, the mean number of primary electrons produced, N_0, is proportional to E_0:

$$N_0 = \frac{E_0}{w} \qquad \text{2.2}$$

where w is the mean energy necessary to produce a primary electron-ion pair and E_0 is the energy of the incident energy.

In the secondary scintillation process, each primary electron produces, on average, N_{VUV} photons, proportional to the energy acquired from the electric field by the electron:

$$N_{VUV} = \eta_S \frac{\Delta E_v}{\varepsilon} \qquad \text{2.3}$$

where η_S is the scintillation efficiency, which depends on E/p in the scintillation region, ΔE_v is the potential energy variation of the electron when it crosses the scintillation region, and ε is the mean excitation energy of the gas.

The number of photoelectrons detected in the photosensor, N_{pe}, is proportional to the solid angle subtended by the photocathode active area relative to the scintillation, Ω, and to the photosensor quantum efficiency, η_Q, according to:

$$N_{pe} = N_0 N_{VUV} \frac{\Omega}{4\pi} T\, \eta_Q \qquad \text{2.4}$$

where T is the window transmittance and N_{VUV} the mean number of VUV photons [8].

The signal at the output of the photosensor is, thus, proportional to the initial X-ray energy which was absorbed in the detector gas medium [11].

2.2.2 Energy Resolution

The response function of the detector is the amplitude distribution, which is typically a Gaussian distribution around the mean value and other features, e.g. due to possible escape radiation from the detector and electronic noise tail. The energy resolution may be given by the ratio of the Full Width at Half Maximum (FWHM) and the centroid of the peak obtained, E_0, of the Gaussian distribution:

$$R = \frac{\Delta E}{E} = \frac{FWHM}{E_0} = 2{,}355 \frac{\sigma_E}{E_0} \qquad\qquad 2.5$$

where E_0 is the centroid position of the Gaussian distribution and σ_E is the standard deviation of the distribution (see figure 2.5).
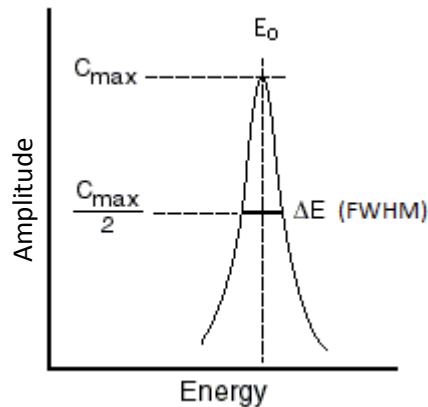
Figure 2.5: Representation of FWHM and E_0 of a peak, necessaries to calculate the energy resolution

The energy resolution of a GPSC depends on the statistical fluctuations in the number of primary electrons, in the number of secondary scintillation photons that reach photosensor and the statistical fluctuations inherent to the amplification process inside the photosensor.

So, for a GPSC equipped with a PMT photosensor, the energy resolution is given by:

$$R = 2{,}355 \sqrt{\frac{F}{N_0} + \frac{1}{N_0}\frac{J}{N_{VUV}} + \frac{2}{N_e}} \qquad\qquad 2.6$$

being N_0 the mean number of primary electrons, F the Fano factor, N_{VUV} the mean number of VUV photons and N_e the mean number of photoelectrons produced in the PMT photocathode because of the scintillation collected there. In equation (2.6), the factor J is introduced to correct for the fact that the distribution is not a Poisson one.

Since the number of secondary scintillation photons produced by one single primary electron is high and the statistical fluctuations are small and *J<<F*, the energy resolution for a collimated beam can be simplified and written as:

$$R = 2{,}355 \sqrt{\frac{F}{N_0} + \frac{2}{N_e}}$$

<div align="right">*2.7*</div>

2.3 Driftless Gas Proportional Scintillation Counter

In a normal GPSC, the interaction of X-rays close to the detector window can produce primary electrons that may be lost to the window. This process results from the diffusion, more important in soft X-rays because they have shorter penetration depths. It was shown that this effect is reduced with the increase of the electric field. Hence, a solution was found to this limitation, a GPSC without drift region.

The driftless GPSC is composed by only one grid near the photosensor. The scintillation region is defined between the radiation window and that grid. The first driftless GPSC was first introduced by Simons and Korte [12].

The main difference between the driftless GPSC and the standard GPSC is the dependence of the output signal on the photon penetration in the scintillation region, i.e., in the driftless GPSC the output signal depends on the distance travelled by the primary electrons produced in this region. To overcome this effect, the signal amplitude is corrected through the relation between the photon interaction position and the pulse rise time. The result is a signal proportional to the absorbed radiation energy, independent of the interaction position or depth [12].

2.4 Electroluminescence

When a primary electron cloud drifts under the action of an electric field, electrons are highly accelerated and gain from the electric field energy enough to excite the xenon atoms but not to ionize them. Excited atoms might return to the ground state and, in the deexcitation, emit photons, secondary scintillation photons.

For pressures above few Torr, excited noble gas atoms create excited dimers, which are molecules composed by two atoms. These dimers decay through radiative emission in the UV region, generating electroluminescence.

The EL mechanism in noble gases, for pressures of 1 atmosphere are given by [13]:

$$X + e- \rightarrow X^* + e- \qquad\qquad 2.8$$

$$X* + 2X \rightarrow X_2^{**} + X \qquad\qquad 2.9$$

$$X_2^{**} + X \rightarrow X_2^* + X \qquad\qquad 2.10$$

$$X_2^* \rightarrow 2X + h\nu \qquad\qquad 2.11$$

Equation 2.1 reflects atom's excitation due to electron impact. In equation 2.2 reflects the dimer formation through a three-body collision process, one atom in the excited state, X* and two atoms in the ground state, 2X. The result is a diatomic molecule in a vibrational excited state, X_2^{**} and a noble gas atom in the ground state, X.

When X_2^{**} collides with an atom, the excimer relaxes to the lowest vibrational state, X_2^* (equation 2.3). X_2^* decays to the X_2 ground state, which is repulsive, emitting a VUV photon, followed by the dissociation of the dimer (equation 2.4).

EL or secondary scintillation gives signals with much larger amplitudes, minimal fluctuations in gain and negligible electronic noise, when compared to primary scintillation. In addition, the amplification of the primary ionization signal through EL results in higher gains and better energy resolution when compared to primary ionization amplification through charge avalanche processes, which is the reason why NEXT chose EL as the primary ionization amplification technique for their detector.

2.4.1 Electroluminescence yield

The addition of molecular impurities to noble gases will produce an increase of the drift velocity and a reduction of the electron diffusion. However, they will reduce the EL yield, i.e. the number of secondary scintillation photons produced per drifting electron per length unit. Therefore, a compromise must be found between the amount of molecular impurities and the reduction of the secondary scintillation.

Vibrational excitation of these molecular impurities at low electron impact energies can compete efficiently with elastic scattering and, as a result, the electron energy may be reduced after a few collisions to values that reduce drastically the chance of exciting the gas [16]. This is one of the reasons to add molecular contaminants (e.g. CH_4, CF_4 or CO_2) to the noble gases.

Electrons may undergo super elastic collisions with vibrational, excited molecular impurities, where electrons will gain energy equal to the excitation energy released by the

molecule (deexcitation) [15]. These gas molecules, called quenching molecules, absorb photons without being ionized, avoiding also recombination of ion-electron pairs.

In the present work different quantities of CH_4 were added to xenon in order to find the optimal mixture (100-x)% Xe + x% CH_4 (x is the percentage of molecular impurity) in such a way that the reduction of the EL yield will not result in significant deterioration of the energy resolution of the detector.

We have Monte Carlo simulations available in the literature [13] for drift velocity, longitudinal diffusion and EL yield, needed to be confirmed experimentally and another parameter needed to be measured, the energy resolution, R (%). The additive percentages were chosen similarly to those used in Monte Carlo simulations (0.5% and 1%).
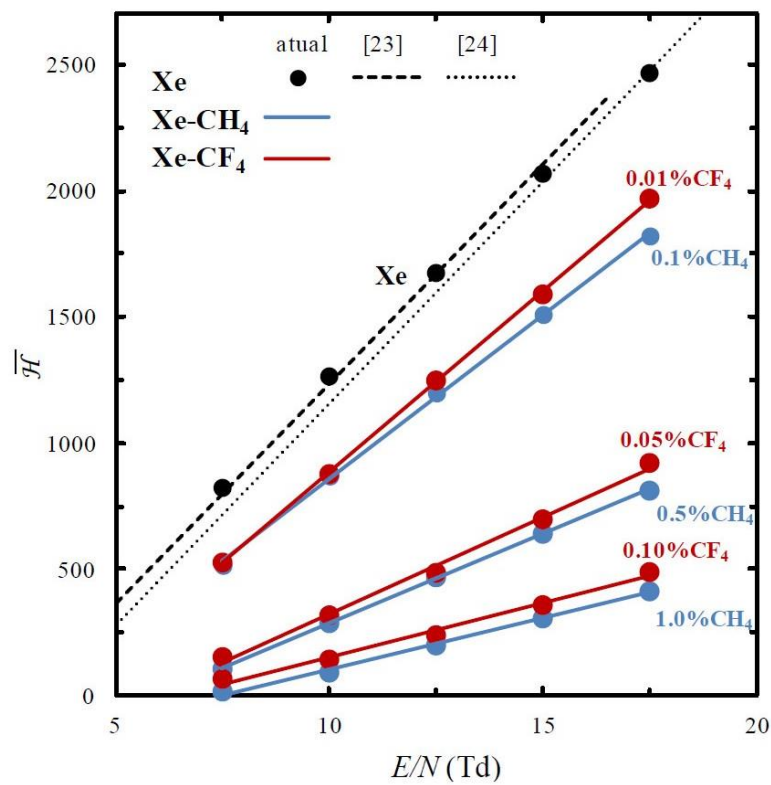
Figure 2.6: Monte Carlo results for the mean number H of EL photons produced in planar geometry under applied reduced electric fields E/N, when one electron drifts across a D=0.5 cm long scintillation region in xenon or in the Xe-CH_4 and Xe-CF_4 mixtures with the indicated η_{CH4} and η_{CF4} molecular concentrations at p = 7600 Torr, T=293 K [15].

2.5 Electron drift velocity

The electron drift velocity is defined as the mass centre velocity of a cloud of free electrons. It is the average velocity that free electrons achieve due to the electric field applied in a certain region, for instance the drift region in a GPSC.

In Y. Kondo et al. [16] the drift velocity of an electron cloud is obtained as:

$$w = \frac{d}{T} \tag{2.12}$$

where d is the distance travelled by electrons and T is the drift time [16]; d is proportional to T since the drift velocity is constant.

As shown in figure 3.6, T is the time that the centre of electron swarm takes from the position where it is absorbed to the position where it reaches the anode.

$$T = T_t - \frac{1}{2}T_f \tag{2.13}$$

where the drift time is related to the total time (T_t) which is the duration of the pulse and fall time (T_f), represented in figure 3.6, according to:
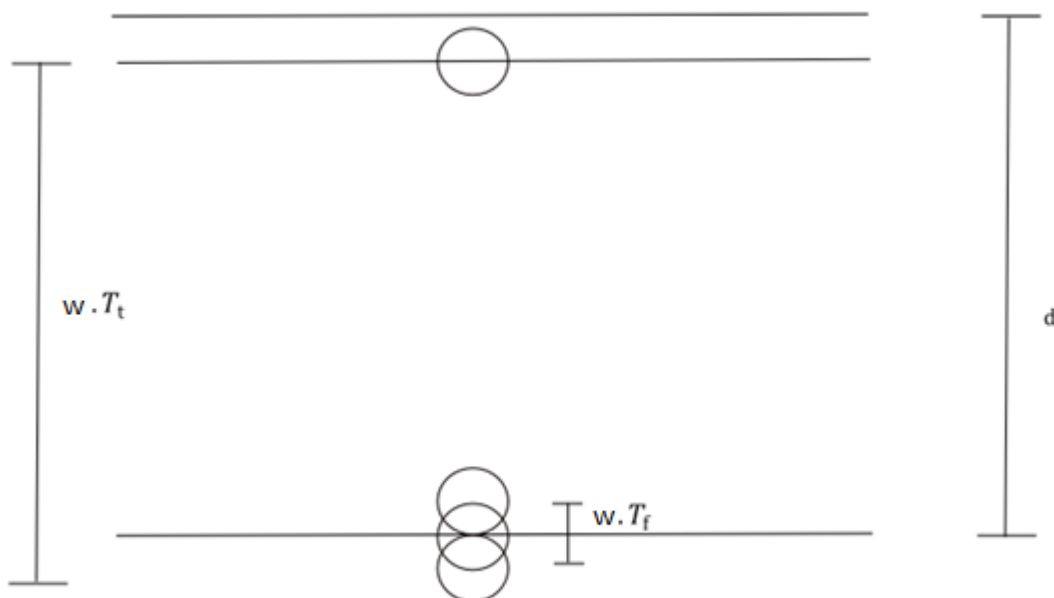
Figure 2.7: Scheme of the electron cloud travelling in a region of thickness d. The circle represents a group of free electrons.

19

The parameters T_t and T_f are determined from the oscilloscope. The circles presented in figure 2.7 are a simplification of the primary electron clouds. This cloud drifts towards the PMT window because of the electric field applied in this region. The duration of the travelled distance is the drift time, T and the signal appears when the frontal part of the cloud touches the PMT window, symbolised by the bottom line in figure 2.7.

Figure 2.8 shows an output signal (top) and the histogram of the total time obtained for 1000 pulses.
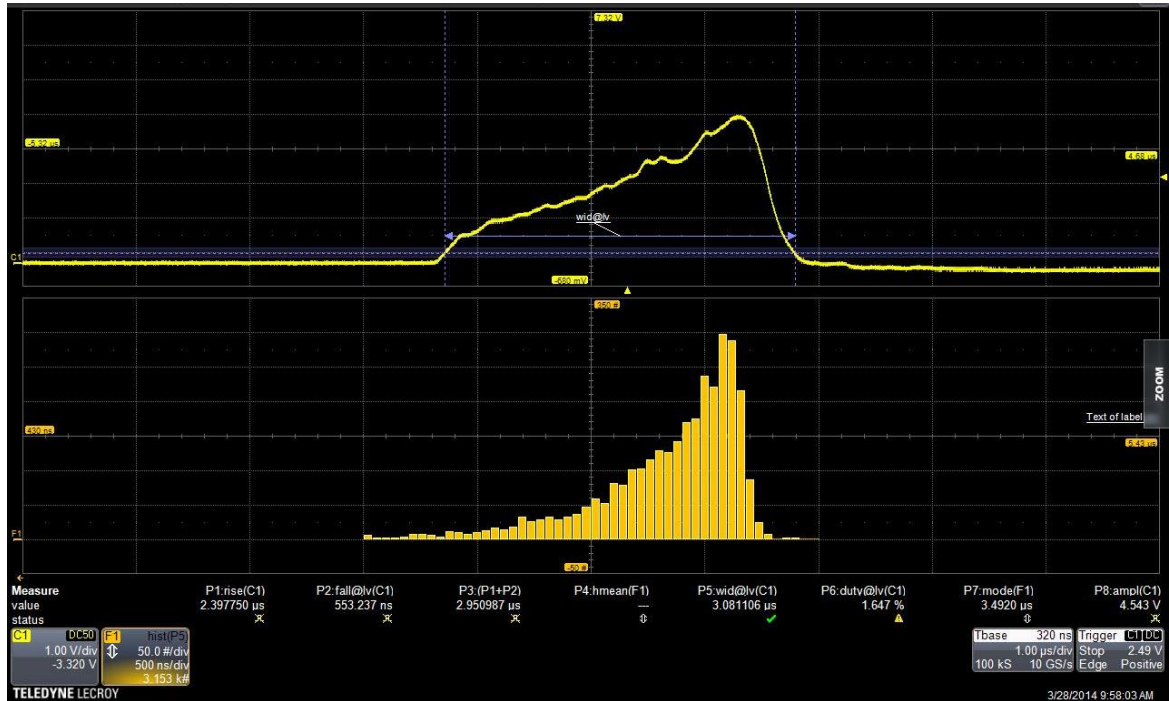
Figure 2.8: Pulse shape (top) and histogram of total time (bottom) obtained with a driftless GPSC for a reduced electric field of 4.5 V/cm/torr with pure xenon.

Figure 2.9 presents another histogram showing the fall time distribution of 1000 pulses.
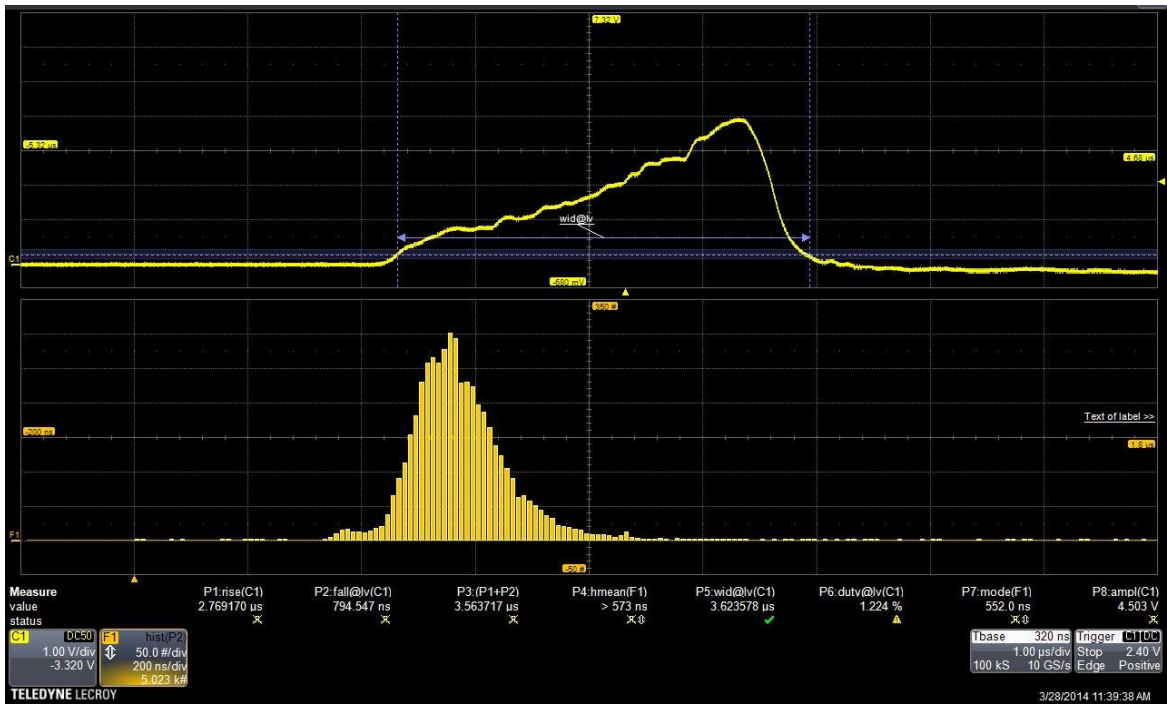

Figure 2.9: Pulse shape (top) and histogram of the fall time (bottom) obtained with a driftless GPSC for a reduced electric field of 4.5 V/cm/torr with pure xenon

The mathematical modes of the histograms of figure 2.8 and figure 2.9 give the total time and the fall time, respectively. In figure 2.8 the total time is 3.49 µs and in figure 2.9 the fall time is 552 ns. Therefore, we can calculate the drift time using equation (2.13) and, considering the travelled distance, the drift velocity is estimated from equation (2.12). In this case, its value is 7.78×10^5 cm/s.

In this work, we use this method to determine the drift velocity in pure xenon and mixtures with small quantities of CH_4 (up to above 2%). Monte Carlo simulations were performed for a gas proportional scintillation counter with amplification achieved through the production of electroluminescence under a charge-multiplication free regime, like in this work. These simulations were made for pure xenon and xenon doped with different percentages of CH_4, and the main results are presented in figures 2.10 and 2.11.
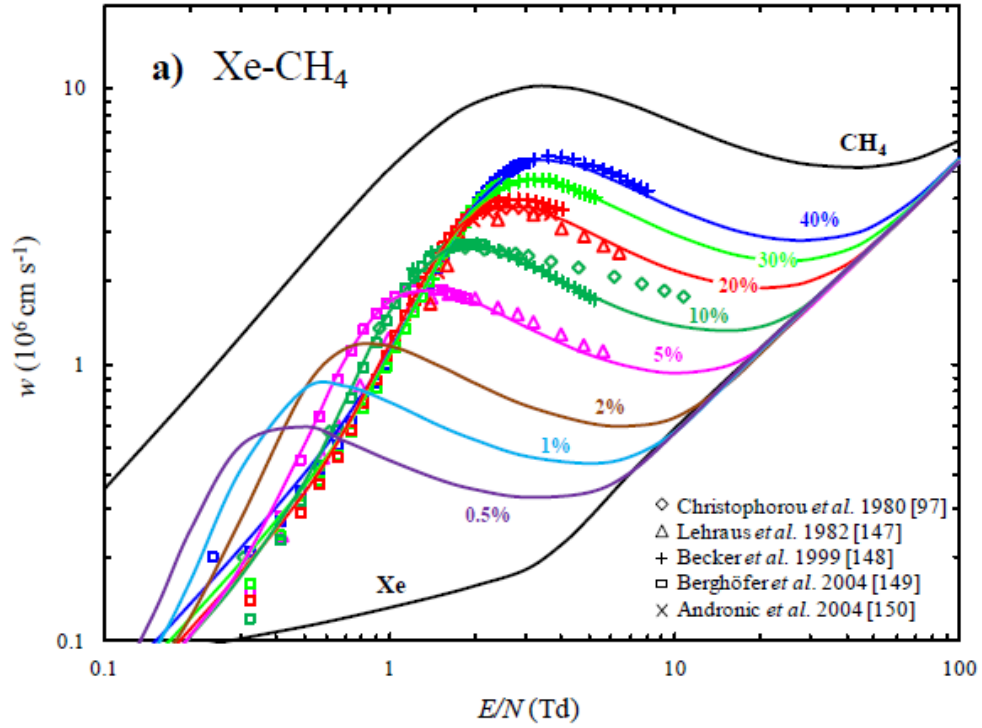
Figure 2.10: Monte Carlo simulation results (curves) and experimental results from literature (symbols) for the electron drift velocity, w, as a function of reduced electric field, E/N, for Xe-CH$_4$ mixtures [15].
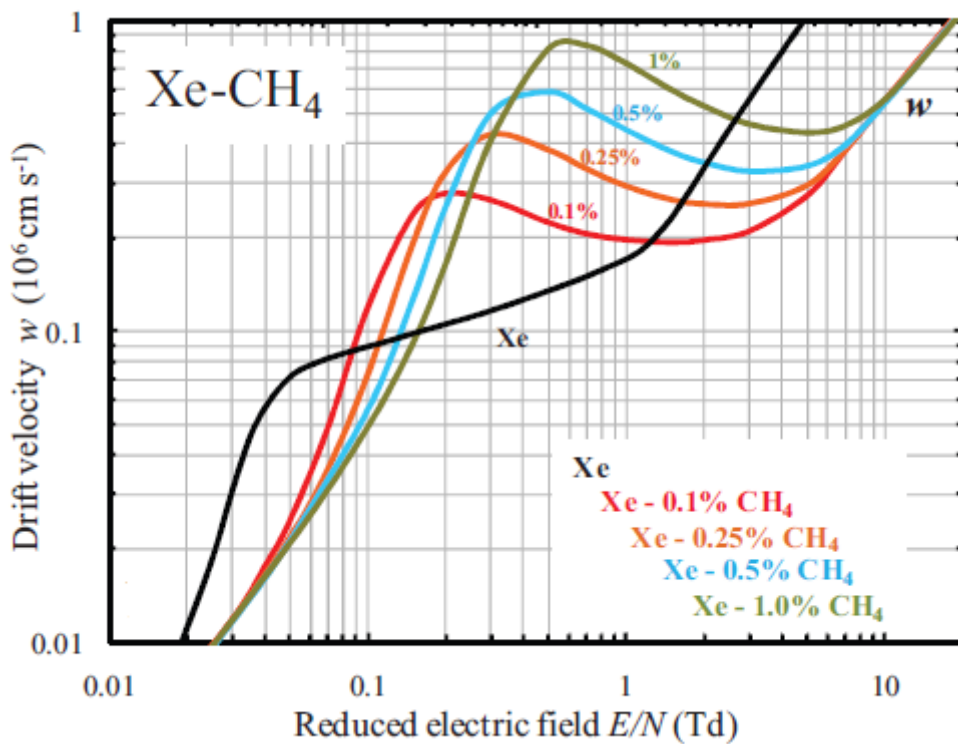
Figure 2.11: Monte Carlo simulations results for the electron drift velocity, w, in xenon and Xe-CH$_4$ mixtures as a function of the reduced electric field, E/N [15].

As seen in figure 2.11, the addition of CH$_4$ to xenon increases the drift velocity, which tends to reach a maximum where *E/N* increases and then exhibits a negative differential conductivity effect, i.e. decrease of *w* at increasing *E/N*.

2.6 Diffusion

There are two types of diffusion, transversal and longitudinal, depending on the direction of the charge motion relative to the electric field. Longitudinal diffusion is an important issue for the NEXT TPC, so we will investigate the behaviour of this parameter in this work.

The longitudinal diffusion parallel to the electric field Hiroki Kusano et al. [17], i.e. in the direction from the window to the PMT. The longitudinal diffusion coefficient is an important transport parameter that can be obtained from w, T_f and T_t through the following equation Hiroki Kusano et al. [17]:

$$D_L = \frac{w^2 T_f{}^2}{2T_t}$$

2.14

Longitudinal and transversal diffusion coefficients can be expressed in terms of two other parameters, the characteristic electron energies ε$_{kL}$ and ε$_{kT}$:

$$\epsilon_{kL} = \frac{eD_L}{\mu}$$

2.15

$$\epsilon_{kL} = \frac{eD_T}{\mu}$$

2.16

In equations (2.9) and (2.9), D$_L$ and D$_T$ are the longitudinal and transversal diffusion coefficients, respectively, *e* is the electron charge and μ is the electron mobility, defined as:

$$\mu = \frac{w}{E}$$

2.17

where *E* is the electric field applied.

Figure 2.12 shows Monte Carlo simulation results for the characteristic electron energies as a function of the reduced electric field for pure xenon and Xe-CH$_4$ mixtures.
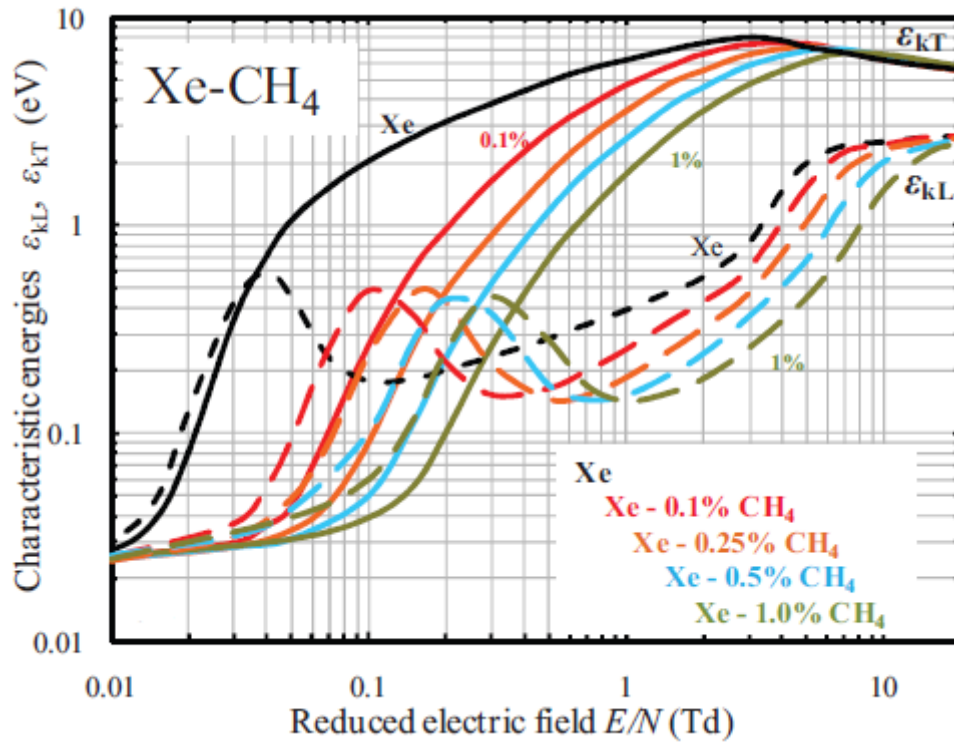
Figure 2.12: Monte Carlo simulation results for characteristic electron energies ε_{kL} and ε_{kT} in xenon and Xe-CH_4 mixtures as a function of the reduced electric field, E/N [15]

In figure 2.12, we can see that the addition of methane to xenon, even in very small percentages, changes the electron longitudinal and transversal diffusion characteristics in the gas, decreasing ε_{kL} and ε_{kT} in general [15].

2.7 References

[1] A.J.P.L. Policarpo, M.A.F. Alves, C.A.N. Conde, *The argon-nitrogen proportional scintillation counter*, Nucl. Instr. Meth. 55 (1967) 105.

[2] C. A. N. Conde, A. J. P. L. Policarpo, M. A. F. Alves, *Gas Proportional Scintillation Counter with xenon and xenon Mixtures*, IEEE Transactions on Nuclear Science 15(3) (1968) 84

[3] C.M.B. Monteiro, J.A.M. Lopes, P.C.P.S. Simões et al., *An argon gas proportional scintillation counter with UV avalanche photodiode scintillation readout*, IEEE Translate Nuclear Science 48 (2001) 1081

[4] S. J. C. do Carmo, F.I.G.M. Borges, C.A.N. Conde, *Performance of agon-xenon Mixtures in a Gas Proportional Scintillation Counter for the 0.1–10 keV X-Ray Region*, IEEE Transactions on Nuclear Science 56 (2) (2009) 898

[5] M.A.F. Alves, M. Salete, S.C.P. Leite et al., *Xenon-krypton mixtures for the gas proportional scintillation counter*, Nuclear Instruments and Methods 144 (3) (1977) 605

[6] T. H. V. T. Dias, F. P. Santos, P. J. B. M. Rachinhas et al., *Xenon-neon gas proportional scintillation counters: Experimental and simulation results*, Journal of Applied Physics 85(9) (1999) 6303

[7] F. Knoll, *Radiation detection and measurement*, John Wiley & Sons Inc 3 (2000) 49

[8] F.P. Santos, *Contadores Gasosos de Cintilação Proporcional para análise por fluorescência de Raios X*, Dissertação de Doutoramento, Departamento de Física, Universidade de Coimbra, Coimbra, Portugal, 1994

[9] A.J.P.L. Policarpo, *The gas proportional scintillation counter*, Space Sci. Instr. 3 (1977) 77

[10] A.J.P.L. Policarpo, *Light production and gaseous detectors*, Physica Scripta 23 (1981) 539

[11] C.M.B. Monteiro*, Contadores Gasosos de Cintilação Proporcional com enchimento a Árgon para Espectrometria de Raios X*, Dissertação de Mestrado, Departamento de Física, Universidade de Coimbra (2006)

[12] D.G. Simons, P.A.J. de Korte, *Soft X-ray energy resolution and background rejection in a driftless gas scintillation proportional counter*, Nuclear Instruments and Methods in Physics Research A A277 (1989) 642

[13] Fabio Favata, Alan Smith, Marcos Bavdaz and Tadeusz Z. Kowalski, Light yield as a function of gas pressure and electric field in gas scintillation proportional counters, Nucl. Instrum. Meth. A 294 (1990) 595.

[15] J. Escada, T.H.V.T. Dias, F.P. Santos et al., *A Monte Carlo study of the fluctuations in xenon electroluminescence yield: pure xenon vs xenon doped with CH_4 or CF_4 and planar vs cylindrical geometries*, JINST 6 (2011) P080068

[16] Y. Kondo, Y. Sekiya, M. Th. EL- Mohandes, *Pulse Townsend Measurement of Electron Swarm Parameters at Low Pressure*, International Journal of Emerging Technology and Advanced Engineering Volume 3 (2013) Issue 11

[17] Hiroki Kusano, José A. Matias-Lopes, Mitsuhiro Miyajima et al., *Electron Mobility and Longitudinal Diffusion Coefficient in High-Density Gaseous xenon*, Japanese Journal of Applied Physics 51 (2012) 116301

3. Experimental system and operation

In the conventional GPSC, the interaction of X-rays close to the detector window produces primary electrons that may be lost to the window, which happens when the electron diffusion towards the window is faster than the drift velocity of the primary electron cloud in the electric field. This process is more probable to occur in soft X-rays, low energy incident photons, because of their low penetration depths. As a consequence of these primary electron losses, the energy resolution increases and the background in the peak region rises due to diffusion.

Other possible degrading effects in conventional GPSCs are the loss of primary electrons to the grid that separates the absorption region from the scintillation region, due to lateral diffusion, and also losses to impurities due to the higher number of inelastic collision in the low electric field of the drift region, for the whole energy range [1].

The fact that a driftless GPSC does not have drift region is one advantage of this type of detector. X-rays are absorbed directly in the scintillation region, which is a way to reduce or eliminate the above mentioned degrading effects because of the higher reduced electric field in the driftless GPSC [2].

However, besides the inexistence of drift region in a driftless GPSC, another difference between a driftless and a conventional GPSC is the dependence of the output signal on the X-ray penetration in the scintillation region, i.e., in a driftless GPSC the output signal depends on the distance travelled by primary electrons produced in this region as they experience different gains. To correct this effect, the signal amplitude is amended taking into account the relation between the photon interaction position and the pulse rise time. The result is a signal proportional to the absorbed radiation energy, independent of the interaction position or depth [1, 3].

3.1 Driftless GPSC: structure and principle of operation

The first driftless GPSC was proposed by Simons and Korte and is presented in figure 3.1. As we can see from the figure, the detector's window is at −HV. The incident radiation, represented by hν, is absorbed in the scintillation region. The electric insulation is achieved with Macor. The PMT window is made of Magnesium Fluorite (MgF$_2$), which converts VUV scintillation into visible light whose wavelength can be detected by the chosen photosensor.
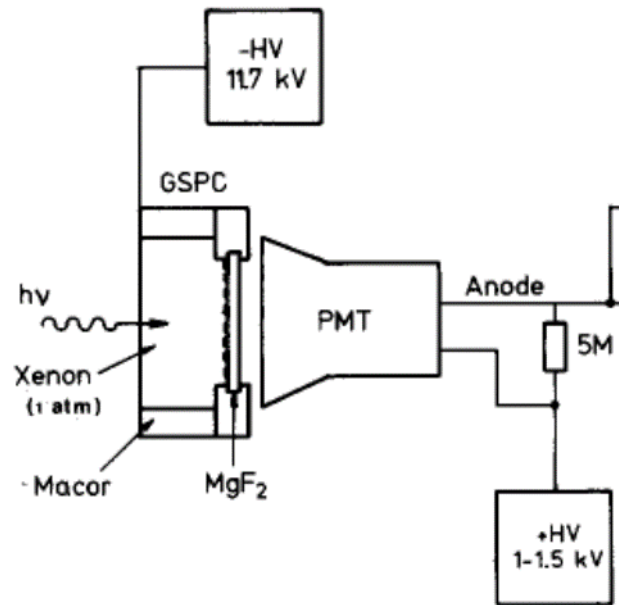
Figure 3.1: GPSC without drift region ("driftless geometry"), proposed by Simons and Korte [4]

As the driftless GPSC does not have a drift region, the radiation is absorbed in the scintillation region. Two processes may occur: photoelectric effect or excitation of xenon atoms. The first process originates primary electrons and the second process is followed by deexcitation, releasing VUV light – primary scintillation.

Therefore, the electrons produced from the interaction of radiation with the gas atoms by photoelectric effect form an electron cloud which is promptly accelerated by the reduced electric field.

The reduced electric field in a driftless GPSC is higher than the xenon excitation threshold (1 V/cm/torr) but lower than its ionization threshold (6 V/cm/torr). The primary electrons travel through the detector, accelerated by the electric field, colliding with xenon atoms. In the collisions, electrons excite the atoms and then, in the process of deexcitation, atoms emit VUV photons, secondary scintillation. The photosensor collects these photons and converts them into a charge signal, similarly to what happen in a standard GPSC [4].

3.2 Experimental Setup

In this work, the driftless GPSC outlined in figure 3.2 was used.

This detector has a 10-cm diameter and 2.5-cm deep scintillation region and is filled with xenon or xenon-CH_4 mixtures at pressures close to 1 atmosphere, continuously purified through

SAES St-707 getters. The upper part of the detector body is made of Macor, which insulates the 8-mm diameter Kapton radiation window and its stainless steel holder. The Kapton, the stainless steel and the Macor are epoxied to each other. The Kapton window is aluminised on the inner side to ensure electrical conductivity. The lower part of the detector is built from stainless steel and is connected to the gas circulation system. The bottom of the detector is a Macor disc epoxied to a 51-mm diameter PMT and to the detector wall. A chromium grid of ~100-μm line width and 1000-μm spacing is vacuum-deposited on the PMT quartz window and connected to the photocathode pin through a continuous chromium film deposited on the lateral surface. The upper and lower parts of the detector are made vacuum-tight by compression of an indium gasket. The Kapton window and holder are kept at negative high voltage, while the chromium grid and the PMT photocathode are kept at 0V. The window holder and the upper Macor piece were designed to ensure a uniform electric field in the scintillation region [1].

The electric field points towards the window, so that electrons travel in the opposite direction, towards the grid (see figure 3.2, number 3). The Macor electrically insulates the window from the remaining detector body.

The photosensor used, a photomultiplier tube (PMT) with quartz window for VUV scintillation light detection, has some advantages such as suitable detection area and quantum efficiency, low dark current and high gain (10^5-10^6), important, for instance, for single photon detection.
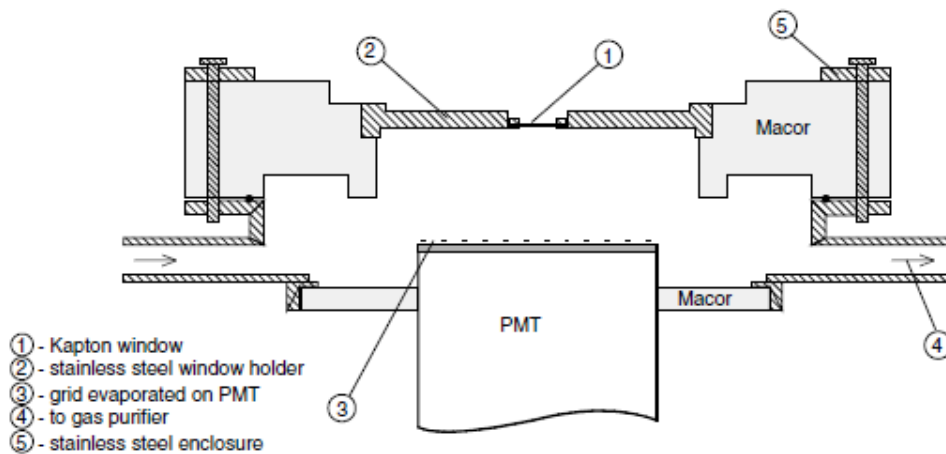
Figure 3.2: Scheme of the driftless GPSC used in this work, already used in [1] and [3].

The charge signal from the PMT was pre-amplified and subsequently formatted with a linear amplifier, with integration/differentiation constants of 5 μs and 50 ns. The formatted pulses were collected with a multichannel analyser (MCA) of 1024 channels and with a digital oscilloscope. More details of the electronic system will be given further on.

Figure 3.3 presents the components of the electronic system used to analyse the pulses from the PMT.

The equipment necessary to operate the detector is composed by two power supplies and a PMT. The HV window power supply has an upper limit of 10kV; applying a voltage higher than this results in discharges. The PMT maximum biasing was set to 800 V.

The window of the GPSC is polarized through an HV source and does not need a low-noise power supply while the PMT power supply must have low noise, in order not to degrade the detector energy resolution.

As can be seen from figure 3.3, the electronic system connected to the driftless GPSC, the preamplifier, a linear amplifier and, finally, a digital oscilloscope and an MCA. The models of each component are listed in table 3.1.
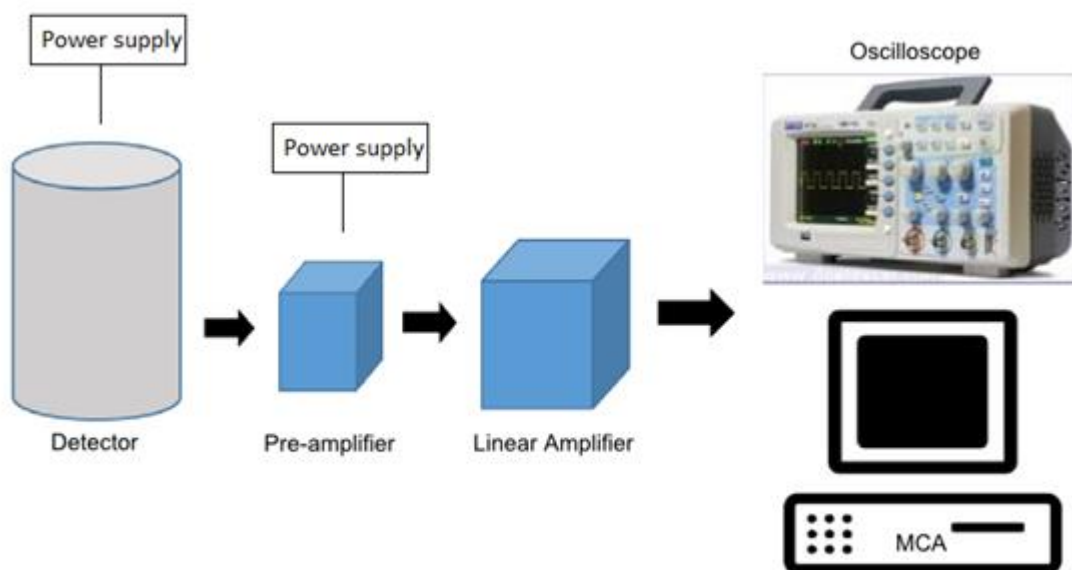
Figure 3.3: Scheme of the electronic detection system

The preamplifier used is from Canberra model 2004, and for the present tests a sensitivity of 9mV/MeV was chosen. The linear amplifier, model HP 5582 A, has variable independent gain and formatting constants (differentiation and integration). The amplifier is connected to both an MCA and a digital oscilloscope.

Table 3.1: List of electronic components used in this work

| Equipment	Brand + Model
NIM basket	ORTEC 4001 A
High Voltage power supplies	For the window: Bertran
	For the PMT: NHQ Fast NHQ 206 L
PMT	
Preamplifier	Canberra 2004 Sensitivity of 9mV/MeV
Linear Amplifier	HP 5582A
Oscilloscope	Lecroy
Multi-channel analyser	PCA-II Nucleus

3.3 Gas system

There are two main gas systems associated to the detector, namely a purifying system with getters and a system to add molecular impurities, represented in figure 3.4.

The first system was used to purify and circulate the gas (see figure 3.4, from valve T1, including T2, T3, to valve T4, in black) and another one to introduce the molecular impurities into the detector (from valve T4 to the CH_4 bottle). Getters (SAES St 707) were used throughout the whole experimental work to purify the gas by convection. During the experiment, getters were maintained at temperatures in the range of $100^{o}C$ to $150^{o}C$.

The reducer allowed the introduction of methane in the impurity system by opening the valve and controlling the amount of CH_4 introduced in the different volumes of the system. With different volumes, it was possible to control the quantity of CH_4 that was introduced in the detector and, this way, we could have different percentages of xenon and CH_4 inside the detector volume.

In figure 3.4 the tube system and other components before valve T1 are not presented because, when the experiment was ready, valve T1 was closed and this part of the system did not interfere with the detector operation. However, the components omitted are important to make vacuum (pumps) in the system and also to introduce the xenon needed from xenon bottle.
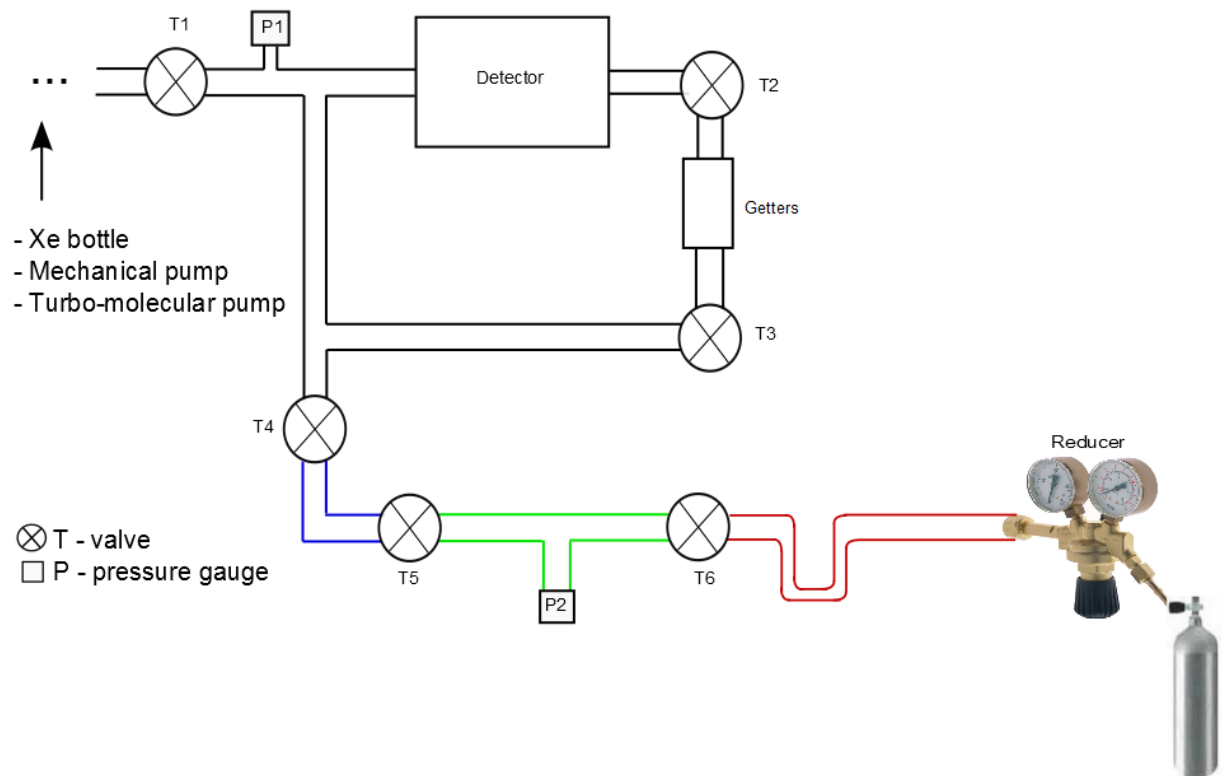
Figure 3.4: Scheme of both gas systems connected to the detector

The U tube presented in figure 3.4 allows the condensation of the methane gas with the help of nitrogen. This is useful when we want to collect the methane gas.

3.3.1 Mixtures

In this work, small quantities of methane were added to the xenon in the detector, through the molecular impurities gas system. To know the percentage x of CH_4 we had to add to have mixtures of (100-x)% Xe + x % CH_4 we need to calculate the ratio of the different volumes in our experimental system, represented by variables V_i defined in table 3.2.

To proceed to the addition of molecular impurities to xenon, we first closed the valve between the detector and the gas impurity system, T4, opened valves T5 and T6, and introduced 1 bar of CH_4 in the tube. Then, we closed valves T5, T6 and reducer. All these volumes, V_5, V_6 and V_7 had the same pressure, 1 bar of CH_4. We also knew the pressure inside V_1, measured with P1 (it was at 0 bar) initially. Afterwards, we opened T4 and, after a while, equilibrium was achieved. From the ideal gas law, $PV= nRT$, where temperature (T) and number of moles (n) were kept constant, we were able to use the following equation:

$$P_i V_i = P_f V_f \qquad\qquad 3.1$$

Table 3.2: Definition of the volumes of the different parts of the experimental system.

Variable	Representing
V_1	Detector volume including getter tube $V_1 = V_2 + V_3$
V_2	Detector volume without getter tube
V_3	Getter tube volume
V_4	Volume of CH_4 system including all the connections $V_4 = V_5 + V_6 + V_7$
V_5	Volume between valves T4 and T5 (in blue)
V_6	Volume between valves T5 and T6 (in green)
V_7	Volume valve T6 and bottle (in red)
V_8	Volume between valves T4 and T6 $V_8 = V_5 + V_6$
V_9	Volume between valve T5 and bottle $V_9 = V_6 + V_7$

Having P_i of *V5* and *V1* and knowing that V_f is *V1+V5* in equation (3.1), we found the ratio between V_1 and V_5. We did similar procedures for all the volumes involved in our experimental setup. Using the relations presented in table 3.2, we obtained the following mathematical relations:

$$V_3 \ = 0.13 \, V_2 \qquad\qquad 3.2$$

$$V_2 \ = 61.3 \, V_5 \qquad\qquad 3.3$$

$$V_2 \ = 17.5 \, V_8 \qquad\qquad 3.4$$

$$V_2 \ = 10.9 \, V_4 \qquad\qquad 3.5$$

$$V_9 \ = 4.6 \, V_5 \qquad\qquad 3.6$$

$$V_1 \ = 70.4 \, V_5 \qquad\qquad 3.7$$

While the main purpose of this work was to study performance features in mixtures of xenon with different amounts of CH_4, 0.5%, 1% and 2%, to obtain these percentages, the following calculations were taken into account.

a) 0.5% of CH4

The detector was filled with pure xenon in volume V_1, at $P_i(Xe)$ measured by pressure gauge P1, with valve T4 closed. By only using volume V_5, filled with CH_4 introduced from the methane bottle, the needed CH_4 pressure to achieve 0.5% in the detector could be estimated. After opening valve T4, volumes V_1 and V_5 reached equilibrium. At this point two different partial pressures have to be considered, one for xenon, and another one for CH_4. Applying equation 3.1 for xenon, the following expression is obtained:

$$P_i(Xe)V_1 + 0V_5 = P_f(Xe)(V_1 + V_5) \qquad\qquad 3.8$$

Using the equation (3.7), the final xenon pressure in the equilibrium between V_1 and V_5 is calculated and presented in table 3.3.

Table 3.3: Initial and final pressures of xenon in volumes V_1 and V_5, for 0.5% of CH_4.

	V₁	V₅
Pᵢ (Xe) (torr)	800	0
P_f (Xe) (torr)	788.8	

$$\frac{P_f(CH_4)}{788.8 + \ P_f(CH_4)} = 0.005 \ \leftrightarrow \ P_f(CH_4) = 3.96 \ torr \qquad\qquad 3.9$$

At this point, the methane pressure that needed to be introduced from the CH_4 bottle could be found using the following relation:

$$0V_1 + P_i(CH_4)V_5 = 3.96(V_1 + V_5) \qquad 3.10$$

The initial pressure, P_i(CH$_4$) that should be added in volume V$_5$ was 286.7 torr (or 0.38 bar). Since the minimum scale division of the pressure gauge of the CH$_4$ bottle was 0.2 bar, we decided to add 0.4 bar (300 torr) of CH$_4$. We put 0.4 bar of CH$_4$ in volume V_4, closed the respective valves, having 0.4 bar in volume V_5.

Table 3.4: Initial and final pressures of CH$_4$ in volumes V_1 and V_5 for 0.5% of CH$_4$.

	V$_1$	V$_5$
P$_i$ (CH$_4$) (torr)	0	300
P$_f$ (CH$_4$) (torr)	4.2	

Finally, the first gas mixture was composed of 0.53% of CH$_4$ and 99.47% of xenon.

b) 1 % of CH$_4$

Since getters had been too warm and CH$_4$ disappeared from the chamber, the detector needed to be refilled with pure xenon. Since with the addition of 0.4 bar of methane in volume V_5 0.5% of CH$_4$ was obtained, to obtain 1% of CH$_4$ 0.8 bar of CH$_4$ needed to be introduced in volume V_5. The xenon pressure before and after opening valve T4 is related by:

$$P_i(Xe)V_1 + 0V_5 = P_f(Xe)(V_1 + V_5) \qquad 3.11$$

Using the mathematical relations (3.1) and (3.13), the final xenon pressure after equilibrium between V_1 and V_5 was obtained, (table 3.5).

Table 3.5 Initial and final pressures of xenon in volumes V_1 and V_5 for 1% of CH_4.

	V_1	V_5
P_i (Xe) (torr)	805	0
P_f (Xe) (torr)	793.73	

For CH_4, the initial and final pressures are related by:

$$0V_1 + P_i(CH_4)V_5 = P_f(CH_4)(V_1 + V_5) \qquad 3.12$$

Thus, the initial pressure that should be added in volume V_5 was 600 torr (or 0.8 bar), (table 3.6). In volume V_4, 0.8 bar of CH_4 was introduced, the respective valves were closed and volume V_5 had a pressure of 0.8 bar inside.

Table 3.6: Initial and final pressures of CH_4 in V_1 and V_5 for 1% of CH_4

	V_1	V_5
Pi (CH_4) (torr)	0	600
Pf(CH_4) (torr)	8.4	

As a result, the mixture was composed of 1.05% of CH_4 and 98.95% of xenon.

c) 2% of CH_4

To add more CH_4 to the previous mixture, we used volume V_6 for CH_4 filling. Applying equation (3.1) to volumes V_1+V_5 and V_6, we obtain for partial pressures of xenon:

$$P_i(Xe)(V_1 + V_5) + 0V_6 = P_f(Xe)(V_1 + V_5 + V_6) \qquad 3.13$$

A final xenon pressure of 768 torr is obtained (table 3.7).

Table 3.7: Initial and final pressures of CH_4 in volumes V_1+V_5 and V_6 for 2% of CH_4

	V_1+V_5	V_6
P_i (Xe) (torr)	793.73	0
P_f (Xe) (torr)	768.02	

The partial pressures for CH_4 are related by:

$$8.4(V_1 + V_5) + 300V_6 = P_f(CH_4)(V_1 + V_5 + V_6) \qquad 3.14$$

For convenience, 0.4 bar of CH_4 was introduced in volume V_6. Table 3.8 shows the final pressure obtained.

Table 3.8: Initial and final pressures of CH_4 in volumes V_1+V_5 and V_6 for 2% of CH_4

	V_1+V_5	V_6
P_i (CH_4) (torr)	8.4	300
P_f (CH_4) (torr)	17.84	

Finally, the mixture was composed of 2.27% of CH_4 and 97.73% of xenon.

3.3.2 Xenon purification system and gas admission

First of all, the line between pumps and valve T1 was pumped down to a pressure of the order of $10^{-7} – 10^{-6}$ mbar and, since the pressure gauge is at some distance from the detector, this pressure could be considered good for xenon purification, because from experience it was clear that inside the detector the pressure is two orders of magnitude above the gauge pressure reading (10^{-5} mbar to 10^{-4} mbar).

The purification of a rare gas inside a closed-system detector is achieved by circulating the gas through getters. To reassure that the getters would be functioning properly, they were reactivated. At first the getter status was tested. Pumping down system and detector, when the pressure reached 10^{-6} mbar, the temperature was increased slowly from 0 to 375°C, with valves

T2 and T3 open. The pressure increased and, after a while, it began to decrease again. At 140°C, the pressure stabilized at 1.3x10^{-6} mbar. After that, the getter tube was closed, by means of closing T2 and T3 and the pressure decreased. This meant that the getters were not purifying but rather releasing what they had already adsorbed.

To reactivate the getters, they were turned on increasing the temperature from 100 to 375°C in steps of 25 or 50°C. The temperature was maintained at 375°C during 45 minutes for getters to be operational at 90-100% [5]. Then, temperature was decreased to 120°C; the pressure was 7.7x10^{-7}mbar. To verify if they were working well, the getter tube was closed by closing valves T2 and T3 and the pressure increased to 8.2x10^{-7} mbar, which meant that the getters were fully operational.

Afterwards, xenon had been frozen down using liquid nitrogen for the purpose, so that impurities and water molecules were withdrawn from xenon. Subsequently, the liquid nitrogen was removed from the xenon bottle, T1 was opened (T2 and T3 were also open) and T4 was closed, and the detector was filled with approximately 800 torr of xenon. After reaching the required pressure, valve T1 was closed and the "excess" of xenon was recollected in the bottle using liquid nitrogen. The pumps were kept running for some time in order to clean and reach a value of the order of 10^{-6} mbar in the main pumping system.

3.4 References

[1] P.C.P.S. Simões, D.S. Covita, J.F.C.A. Veloso et al., *A new method for pulse analysis of driftless-gas proportional scintillation counters*, Nuclear Instruments and Methods in Physics Research A 505:1-2 (2003) 247

[2] D.G. Simons, P.A.J. de Korte, *Soft X-ray energy resolution and background rejection in a driftless gas scintillation proportional counter*, Nuclear Instruments and Methods in Physics Research A A277 (1989) 642

[3] D.S. Covita, P.C.P.S. Simões, L.M.P. Fernandes et al., *The X-ray performance of a driftless gas proportional scintillation counter using short shaping-time constants for pulse analysis*, Nuclear Instruments and Methods in Physics Research A 516 (2004) 134

[4] D.G. Simons, P.A.J. de Korte, *Soft X-ray energy resolution and background rejection in a driftless gas scintillation proportional counter*, Nuclear Instruments and Methods in Physics Research A A277 (1989) 642

[5] SAES Group, http://www.saesgetters.com/

4. Experimental Results

In this work we also aimed at observing primary scintillation pulses produced by X-rays from ^{55}Fe and ^{109}Cd radioactive sources that interact in the filling gas of the GPSC. Electroluminescence measurements were performed as well, such as amplitude and energy resolution of secondary scintillation pulses that result from the interaction of 5.9 keV X-rays emitted by a ^{55}Fe radioactive source.

A thin chromium film was placed between the radioactive source and the detector radiation window to absorb efficiently the most part of the 6.4 keV X-rays (Mn K_β line), which are emitted by the ^{55}Fe together with the 5.9 keV X-rays (Mn K_α line) [1], which allows achieving better energy resolution.

4.1 Primary scintillation

Primary scintillation is produced in xenon during the formation of the cloud of primary electrons [1]. When X-rays interact with xenon atoms, they ionize those atoms, which emit photoelectrons and Auger electrons. These electrons further excite and ionize other gas atoms until they thermalize. In the deexcitation process, VUV radiation is emitted, the primary scintillation.

With the driftless GPSC we could only observe secondary scintillation with the digital oscilloscope (figure 4.1), while the amplitude of primary scintillation pulses was too low to be distinguished from the noise, independently of the constants used. The spur presented in the rising edge of the pulse shown in figure 4.1 is not primary scintillation, but rather an artifact of the digital oscilloscope, which is always present as it follows the trigger.
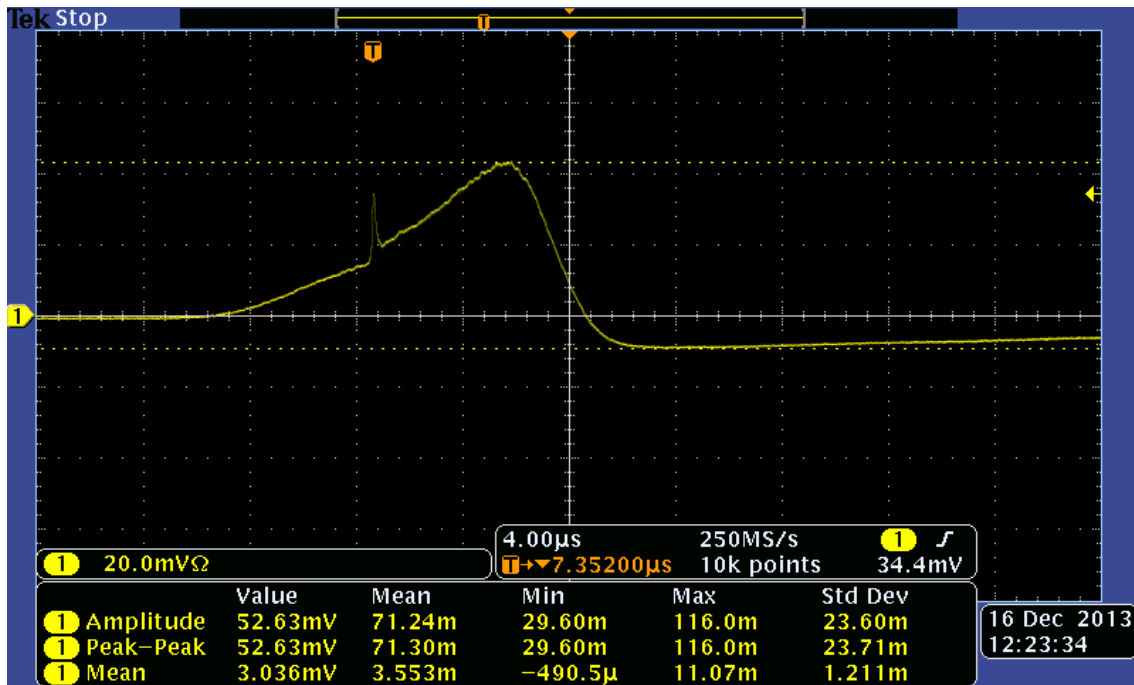
Figure 4.1: Typical secondary scintillation pulse observed with the oscilloscope, after averaging 512 pulses, for 5.9-keV X-rays interacting in gaseous xenon for a PMT bias voltage of 650 V, E/p of 2.8 V/cm/torr and a shaping constant of 50 ns.

Since primary scintillation pulses could not be detected with the digital oscilloscope, the electronic settings were optimized in order to try to detect these pulses with the MCA. Knowing that the ratio between the secondary and the primary scintillation amplitudes is of the order of 10^3 [1], the amplifier gain and the PMT voltage were increased one thousand times relative to the gain used for secondary scintillation measurements. To increase this gain to about 1000 times, the PMT maximum biasing was set to 800 V and the coarse gain of the linear amplifier was set to its maximum.

Several spectra were collected and analyzed, but background was varying significantly as a function of time because of variation in the noise rate.

Figure 4.2 presents the distribution obtained with the ^{55}Fe and ^{109}Cd radioactive sources, together with a background distribution, without source.
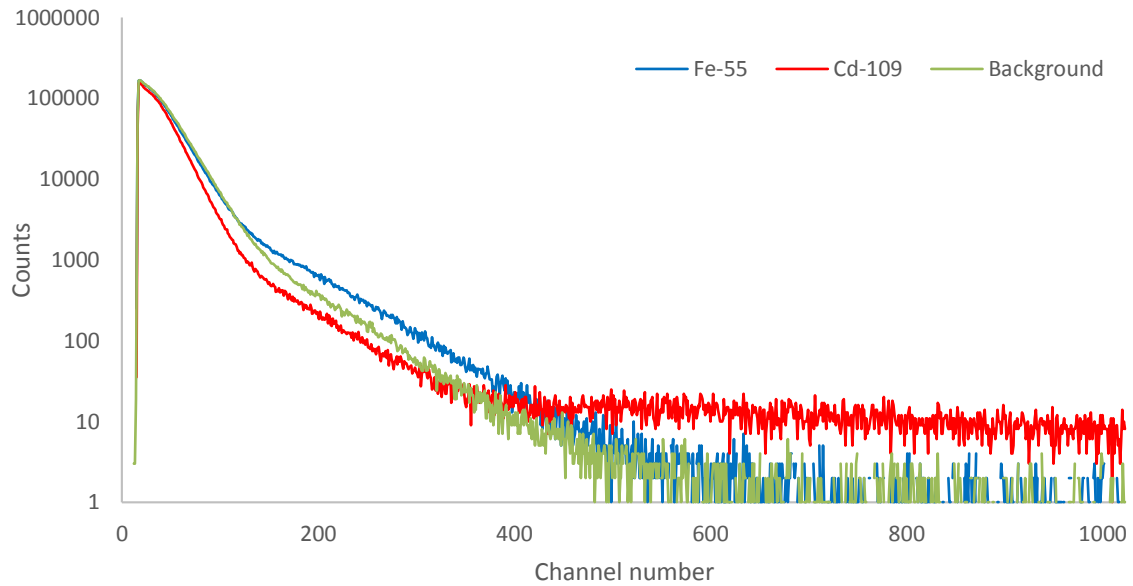
Figure 4.2: Pulse-height distributions (raw spectra) and background obtained for 5.9-keV and 22.1-keV X-rays from ^{55}Fe and ^{109}Cd radioactive sources, respectively, without electric field applied to the scintillation region, for a PMT bias voltage of 800V and for shaping constants of 5 μs in the HP amplifier.

Figure 4.3 is obtained from figure 4.2 subtracting the background distribution from the distributions obtained with the sources. However, the background distribution includes noise that may vary significantly. The noise overlaps the primary scintillation for 5.9 keV X-rays and it is not possible to isolate a full pulse-height distribution for the primary scintillation, but only its high-energy tail. This will not be sufficient for the study of the impact of the addition of CH_4 on the primary scintillation yield. Therefore, we gave up this purpose.
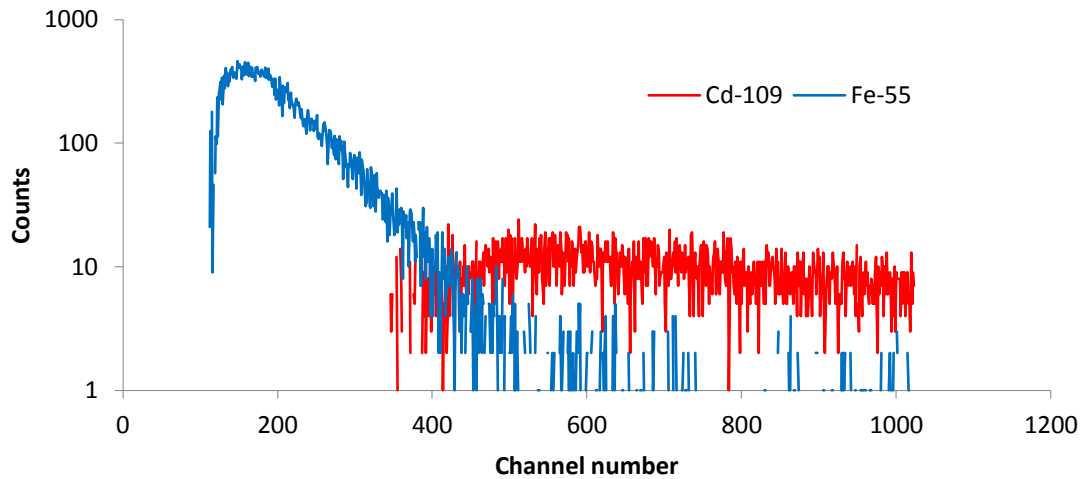
Figure 4.3: Pulse-height distribution obtained for 5.9-keV and 22.1-keV X-rays absorbed in the detector after background subtraction, without electric field applied to the scintillation region, for a PMT bias voltage of 800V and for shaping constants of 5 μs .

4.2 Pure xenon

We studied the energy resolution, amplitude, the drift velocity and the longitudinal diffusion of our experimental results for pure xenon and mixtures of xenon with a small amount of CH_4, typically below 5%. In the case of pure xenon, we considered different temperatures for the getters, from 100 to 195°C and pressures of 800 torr and 1000 torr, as is shown in table 4.2.

Table 4.1: Experimental runs for pure xenon

| Run nº.	Xe pressure (torr)	$T_{getters}$ (°C)
1	1008	195
2	798	150
3	810	120
4	804	100

4.2.1 Energy resolution and amplitude

As seen in figure 4.4, the pulse-height distribution was fitted with a fitting program which calculated the centroid position and the full width at half maximum values. This distributions is not Gaussian but a convolution of a Gaussian function on the right half, with an

exponential function on the left part towards the low energy region. The method fits the right half and a small slab of the left part of the distribution to a Gaussian.
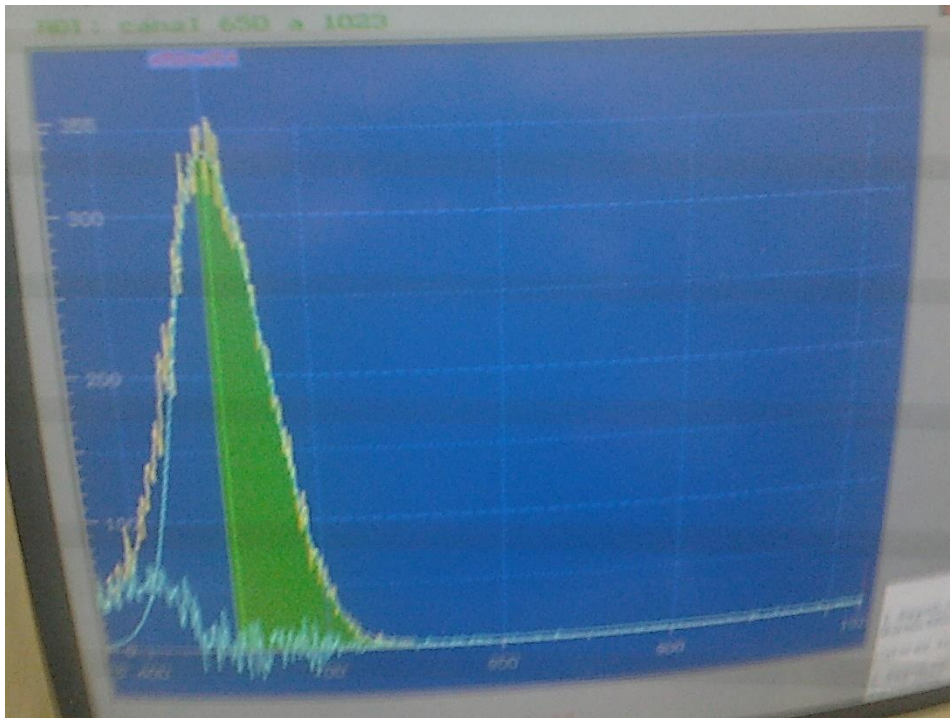
Figure 4.4: MCA spectrum fitted for a pulse-height distribution for 5.9 keV X-rays absorbed in the xenon driftless GPSC. The PMT was biased to 800 V, the reduced electric field was 4.3 V/cm/torr and formatting constants of 5 µs.

Figure 4.5 shows a typical pulse-height distribution obtained for pure xenon for 5.9 keV X-rays.
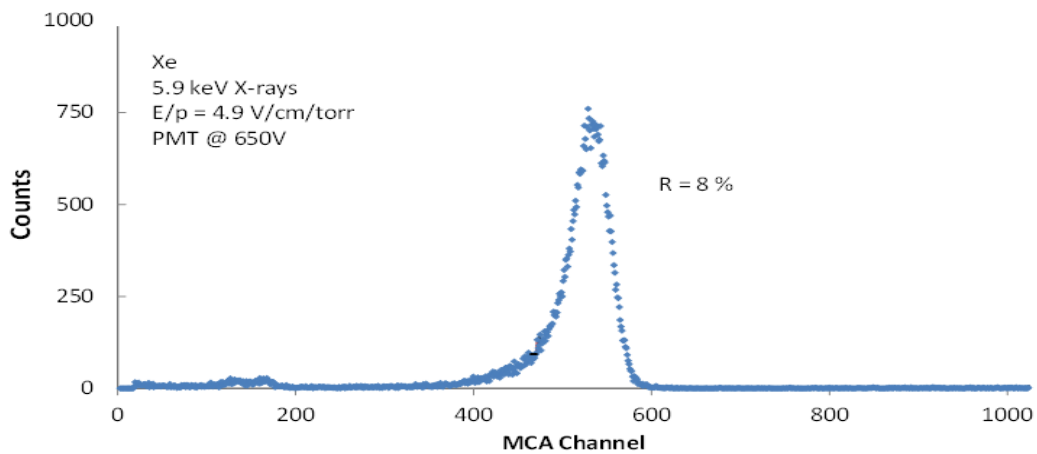
Figure 4.5: Pulse-height distribution for 5.9 keV X-rays absorbed in the xenon driftless GPSC. The PMT was biased to 650 V, the reduced electric field was 4.9 V/cm/torr and formatting constants of 5 µs.

The studies made for pure xenon were, for shaping constants of 5 μs and 50 ns:

- amplitude and energy resolution as a function of reduced electric field maintaining the PMT bias voltage constant;

- amplitude and energy resolution as a function of PMT bias voltage maintaining the reduced electric field constant

- Comparison of the energy resolution between energy spectra of 5 μs and 50 ns.

Experimental run number 1

Figure 4.6 presents the relative amplitude and energy resolution as a function of E/p of the driftless GPSC filled with xenon at a pressure of 1008 torr for shaping constants of 5 μs and 50 ns, while the temperature of the getters was set to 195°C.

For 5 μs the signal collected corresponds to the total amount of EL produced in the whole scintillation region while for 50 ns only the EL produced in the last very small slab of the scintillation region close to the photosensor contributes to the signal and, consequently, the statistical fluctuations in the EL production, for the same E/p, are more important in the latter case and that's why we used 5 μs as shaping constant.
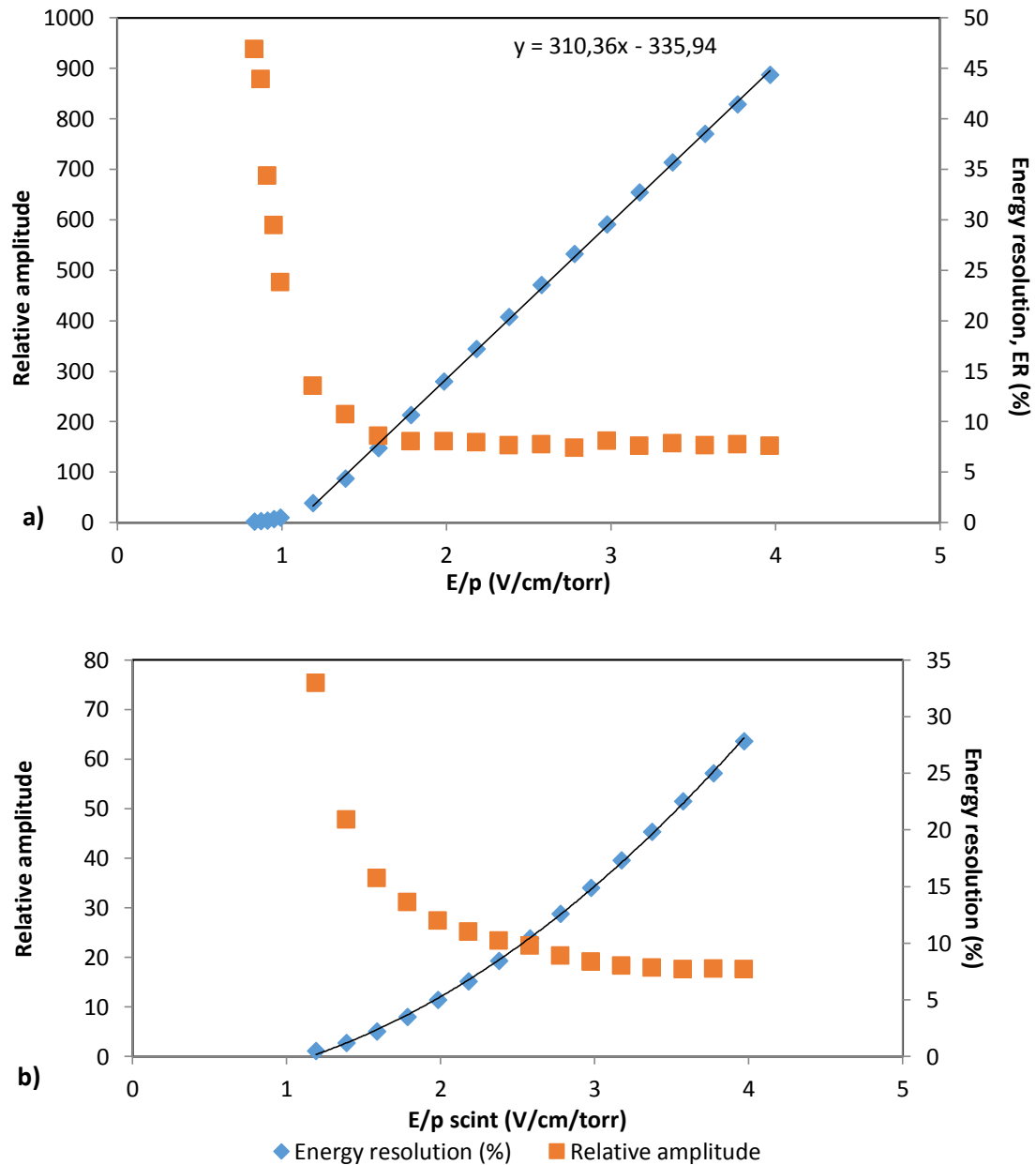
Figure 4.6: Relative amplitude and energy resolution as function of the reduced scintillation electric field, E/p scint for 5.9-keV x-rays from a [55]Fe source, for a xenon pressure of 1008 torr, a constant PMT bias voltage of 650 V and formatting constants of **a)** 5 μs; **b)** 50 ns. The temperature of the getters was around 195°C.

From the graph of the amplitude as a function of E/p the scintillation threshold can be deduced, being the E/p value corresponding to the intersection of the straight line fit to the amplitudes (figure 4.6a) with the E/p scintillation axis, i.e., the value of E/p where the EL starts to be produced. This value was found to be ~1.0 V/cm/torr for pure xenon, which is in agreement with the values reported in the literature [2].

It is clear, from figure 4.6 a), that in the region below the scintillation threshold, the signal amplitude is constant since there is no production of EL, i.e., there are no processes of light gain that depend on E/p.

The number of photons produced per primary electron that reach the scintillation region is proportional to the E/p $_{scint}$ [3]. Therefore, for the same PMT bias voltage, the higher the E/p, the higher the secondary scintillations and, consequently, the larger the signal amplitude detected by the PMT.

In the scintillation region, the relative amplitude increases linearly, between the excitation and the ionization thresholds, for long shaping constants (see figure 4.6 a)).

Also for 5 μs (figure 4.6 a)), the energy resolution decreases rapidly as E/p increases in the scintillation region, especially after reaching the excitation threshold. The energy resolution stabilizes after ~1.5 V/cm/torr. This is due to the strong increase in the quantity of EL produced in the scintillation region. Since primary electrons gain more energy from the electric field, they produce more quantity of scintillation.

From a certain value of E/p on and until the onset of ionization, the quantity of EL is high enough for the statistical fluctuations inherent to the scintillation processes not to be significant for the detector performance. This explains why the energy resolution stabilizes after a certain value of E/p.

For 50 ns, the energy resolution behavior is similar, although decreasing slower than for 5 μs, with the same variation of E/p. For 5 μs the signal collected corresponds to the total amount of EL produced in the whole scintillation region while for 50 ns only the EL produced in the last very small slab of the scintillation region close to the photosensor contributes to the signal and, consequently, the statistical fluctuations in the EL production, for the same E/p, are more important in the latter case. The amplitude increases faster than linearly with E/p.

Figure 4.7 presents the ratio between the amplitudes of the secondary scintillation signal as a function of the scintillation reduced electric field, E/p$_{scint}$, for the shaping constants of 5 μs and 50 ns. That ratio is diminishing with increasing E/p, effect explained by the reduction of the size of the primary electron cloud, i.e., the reduction of the diffusion with the increase of E/p.

While for the shaping constant of 5 μs the signal amplitude results from the total amount of secondary scintillation produced and, therefore, is proportional to the E/p value applied to the region, for the shaping constant of 50 ns it is the secondary scintillation produced when the scintillation collected by the PMT has its maximum value that defines the signal amplitude.

In spite of the fact that the mean number of photons produced by the primary electrons is constant in all instants, the number of photons collected by the PMT increases with the

approximation of the primary electron cloud to the PMT window, since the solid angle subtended by the PMT increases. This is because the secondary scintillation collected by the PMT is maximum when the first electrons from the primary electron cloud reach the PMT window. In this situation, the average distance from the cloud to the PMT is, in first approximation, equal to the radius of the cloud. Since the diffusion of the cloud, i.e., its length, decreases with E/p, the mean distance from the PMT to the primary electron cloud reduces when E/p increases. The solid angle subtended by the PMT increases also, and the quantity of secondary scintillation collected by the PMT, add to the linear increase of the average secondary scintillation produced as a function of E/p. As a result, the signal variation with E/p, for the shaping constant of 50 ns, is faster than the linear variation of the secondary scintillation as function of E/p for 5 µs.
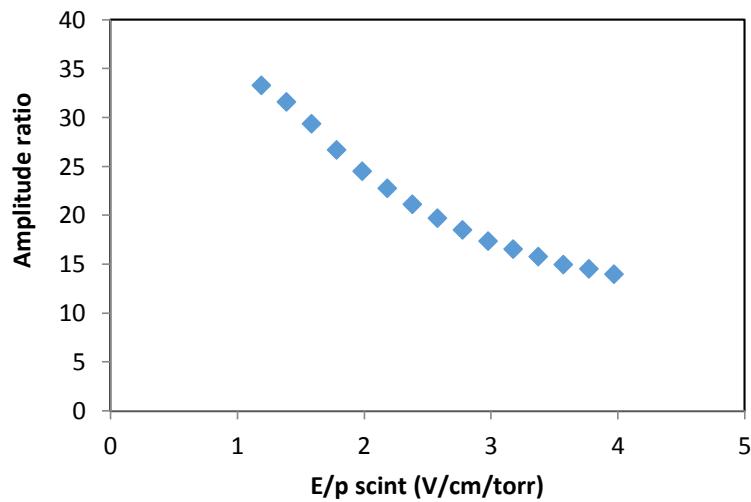
Figure 4.7: Ratio of the amplitudes for the shaping constants of 5 µs and 50 ns, and for 1008 torr.
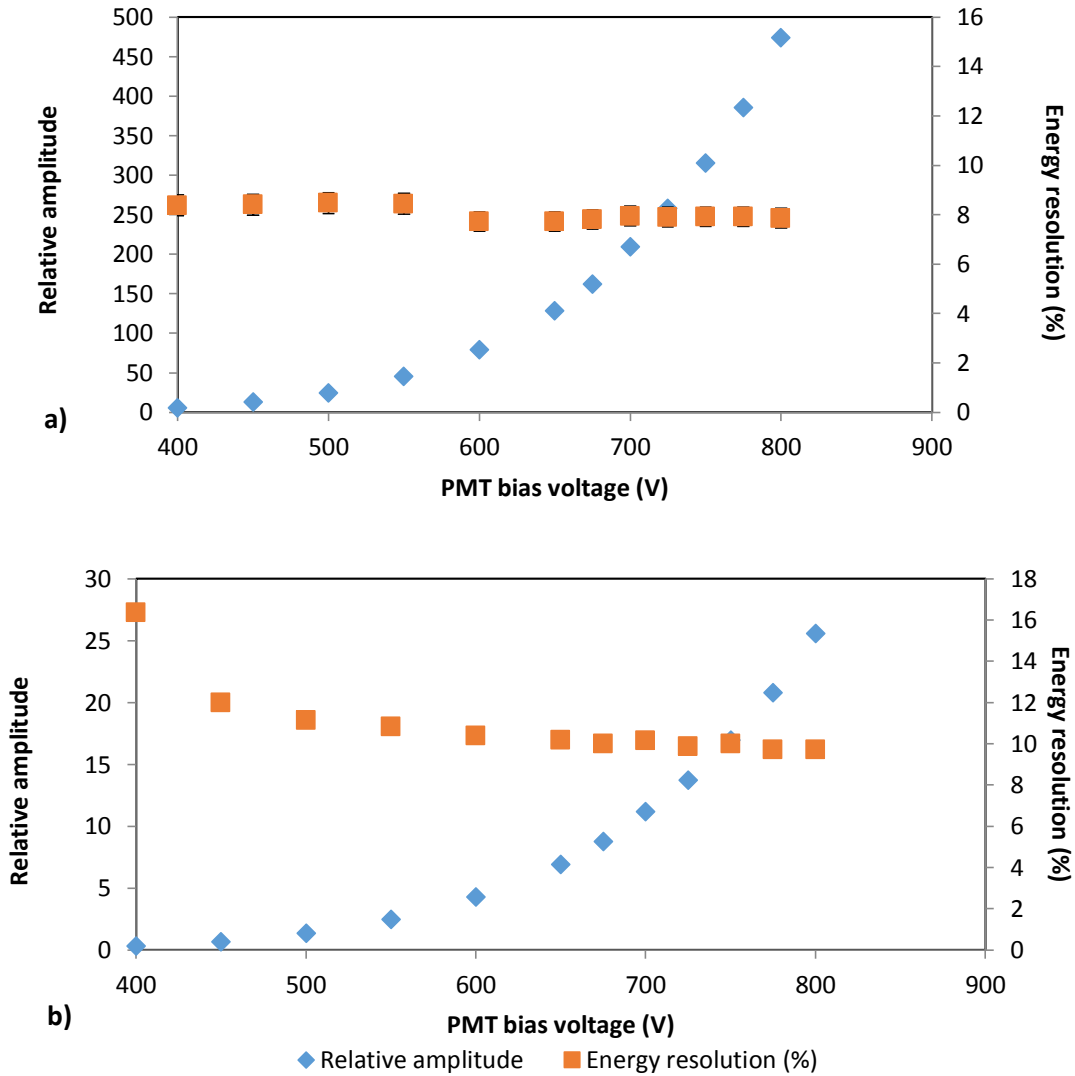
Figure 4.8: Relative amplitude and energy resolution as a function of PMT bias voltage for a constant scintillation E/p of 2.8 V/cm/torr for pure xenon and shaping constants of **a)** 5 us; **b)** 50 ns.

The behavior in figure 4.8 is typical. Maintaining the same E/p, the scintillation does not increase, only the signal amplification rises with increasing PMT bias voltage (PMT gain).

Increasing the PMT gain, the energy resolution decreases, and from 600V to 800V is almost constant because the PMT voltage is already optimized at 600V, considering the energy resolution. Comparing, for instance, the point corresponding to 650 V of PMT bias voltage, the energy resolution is approximately 8% (see figure 4.8 a)) and compares to figure 4.6 a) for 2.8V/cm/torr.

In figure 4.9 a comparison is made between signal amplitudes as a function of PMT bias voltage for 5 μs and 50 ns and for a scintillation reduced electric field of 2.9 V/cm/torr. The

behavior described is equivalent for the two shaping constants. As the PMT voltage increases, the gain also increases; consequently, the signal amplitude is higher.
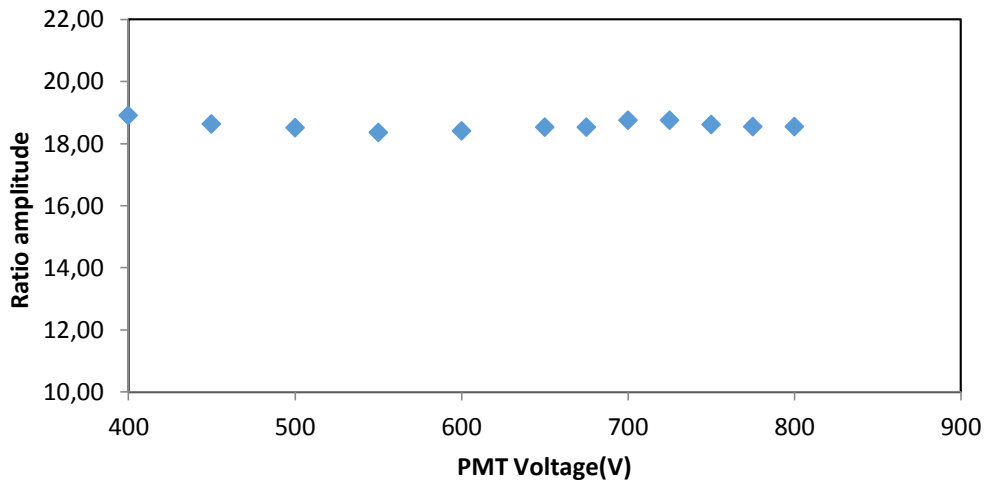
Figure 4.9: Ratio of signal amplitudes for shaping constants of 5 µs and 50 ns, for a pressure of 1008 torr and a constant scintillation E/p of 2.8 V/cm/torr.

As can be seen from figure 4.9, the ratio between the amplitudes for the short and the long shaping constant is approximately constant with the variation of the PMT bias voltage for a constant scintillation E/p value, i.e., the signal amplitude increases in the same proportion for both cases, as the PMT gain increases, being the EL production constant.

Figure 4.10 shows the pulse-height distributions obtained in the MCA for 5 µs and 50 ns shaping constants, for a reduced electric field of 4V/cm/torr and PMT bias voltage of 650 V.
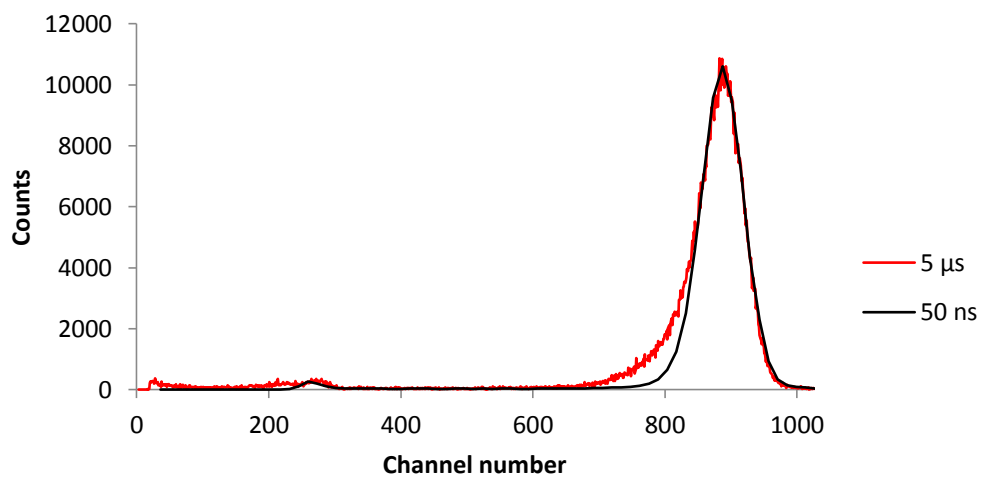

Figure 4.10: Pulse-height distributions obtained with pure xenon and the getters operating at 195°C for 5 µs and 50 ns shaping constants, for a reduced electric field of 4V/cm/torr and PMT bias voltage of 650 V.

As shown in figure 4.9, there is a large similarity between the pulse-height distributions for shaping constants of 5 µs and 50 ns. The energy resolution is approximately equal for both cases, but for 50 ns the pulse-height distribution is noticeably, because it does not present the higher low-energy tail.

Run number 2

The studies of run number 1 were repeated for different operation temperatures of the getters. Run number 1 consists in analyzing pure xenon at 150°C with a filling pressure of 798 torr.
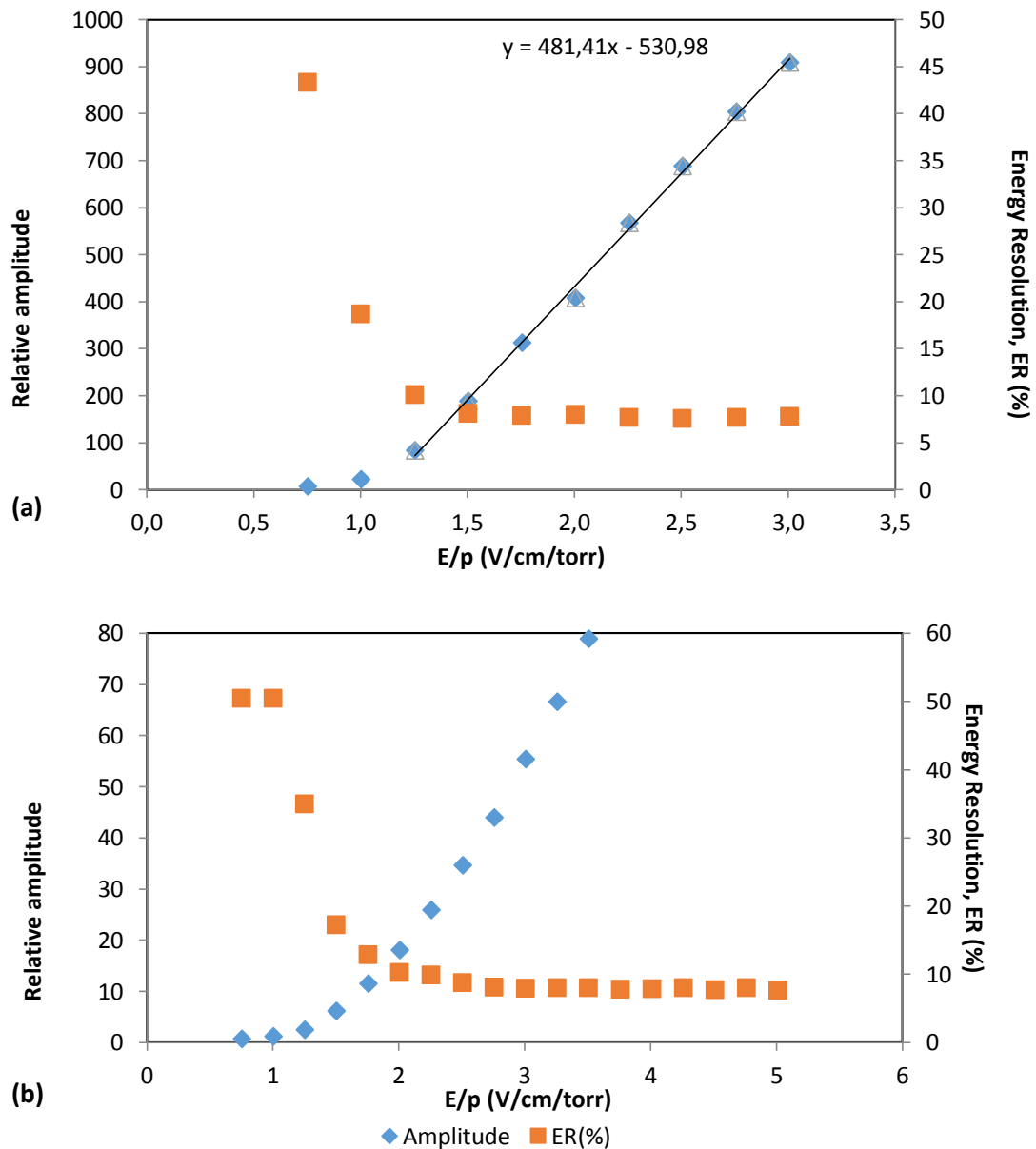
Figure 4.11: Relative amplitude and energy resolution as a function of the reduced electric field, E/p, for pure xenon with getters operating at 150°C, for 5 µs **(a)** and 50 ns **(b)** shaping constants. A PMT bias voltage of 800 V was used and the gas pressure was 798 torr.

Figure 4.10 shows the variation of amplitude (centroid channel in the MCA) and energy resolution, R (%), for 5.9 keV X-rays as a function of the scintillation reduced electric field, E/p, for a filling pressure of 798 torr, with the getters operating at 150°C and for shaping constants of 5 μs and 50 ns. The behavior of these two figures are typical [4, 5].

In figure 4.11, the amplitude increases linearly with increasing scintillation E/P and the energy resolution decreases exponentially with it, for the same voltage applied to the PMT. The linear trend of the amplitude is the expected behavior for 5 μs.

The energy resolution is higher for E/p values lower than 1V/cm/torr, the xenon excitation threshold, since the electric field is not enough to excite the xenon atoms.

In the E/p range of 1 to 3 V/cm/torr (see figure 4.10), the energy resolution is almost 8% and constant. The same behavior is visible in the energy resolution for shaping constants of 50 ns (see figure 4.10) and remains constant for E/p values in the range of 1 to 5 V/cm/torr. This linear region extends to an E/p of 6V/cm/torr, the xenon ionization threshold.

The expected behavior of the energy resolution for E/p values higher than 6 V/cm/torr is that it increases, because the scintillation E/p exceeds the xenon ionization threshold, hence the energy resolution gets worse.

The xenon excitation thresholds ~1.0 V/cm/torr (see figure 4.10 a).

Run number 3

Run number 3 consists in analyzing pure xenon at 120°C with a filling pressure of 810 torr.

Figure 4.11 presents the amplitude and energy resolution obtained for pure xenon with getters operating at 120°C with a filling pressure of 810 torr for 5.9 keV X-rays as function of the scintillation reduced electric field, E/p scint.
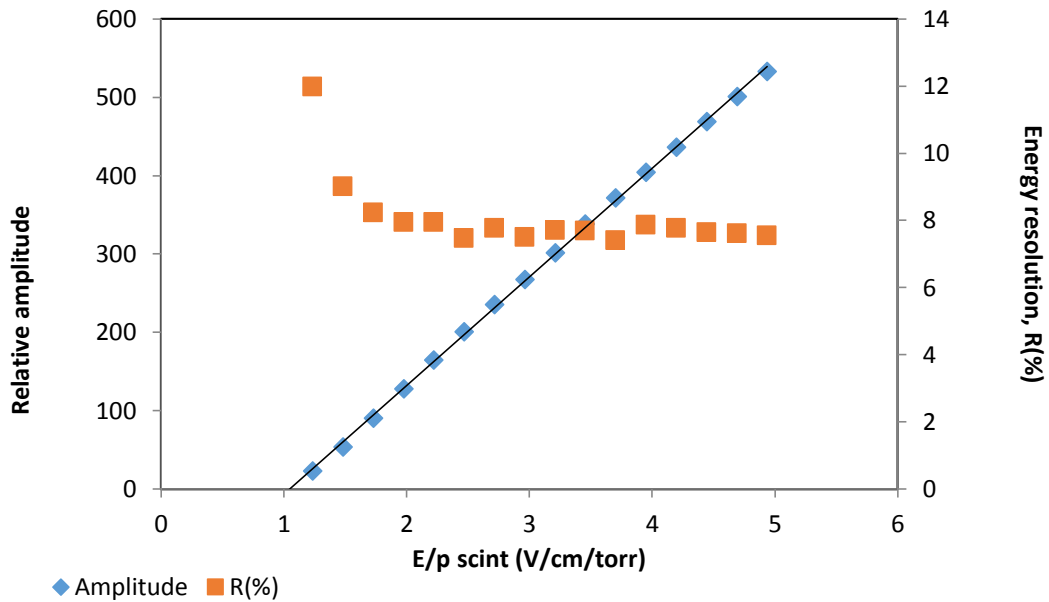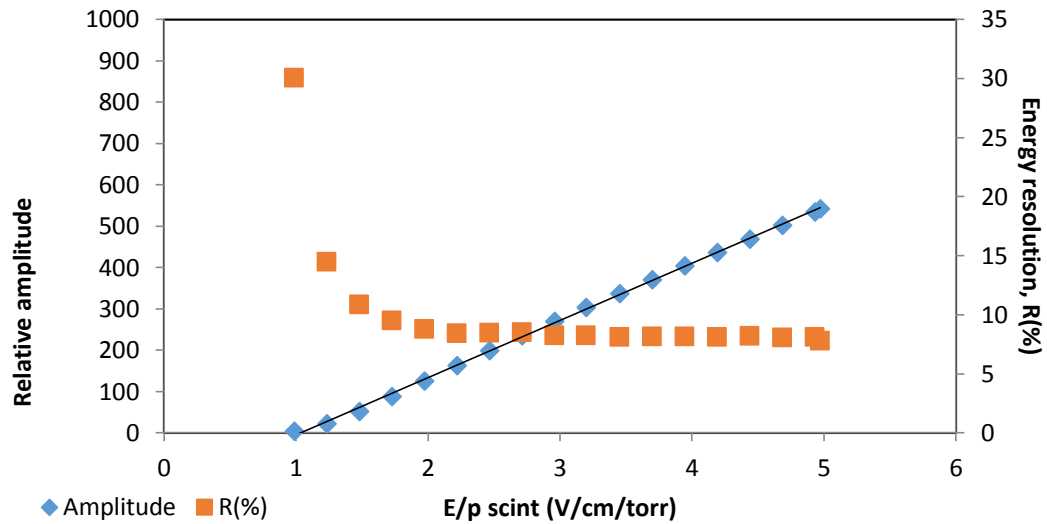
Figure 4.13: Relative amplitude and energy resolution as a function of reduced electric field, E/p_{scint}, for 5.9 keV X-rays for pressure of 810 torr of pure xenon at 120°C and for 5 µs with a constant PMT bias voltage of 650 V.

Figure 4.11 had the typical behavior mentioned in the studies above. For 5µs, from the intersection of the linear trendline of the amplitude as function of E/p with the E/p axis, one can conclude that the xenon excitation threshold is ~1.0 V/cm/torr for 120°C.

Run number 4

Run number 4 consists in analyzing pure xenon at 100°C with a filling pressure of 804 torr.

Figure 4.14: Relative amplitude and energy resolution as a function of reduced electric field, E/p, for pure xenon at 100°C with a filling pressure of 804 torr, for a constant PMT bias voltage of 650 V and shaping constant of 5 μs.
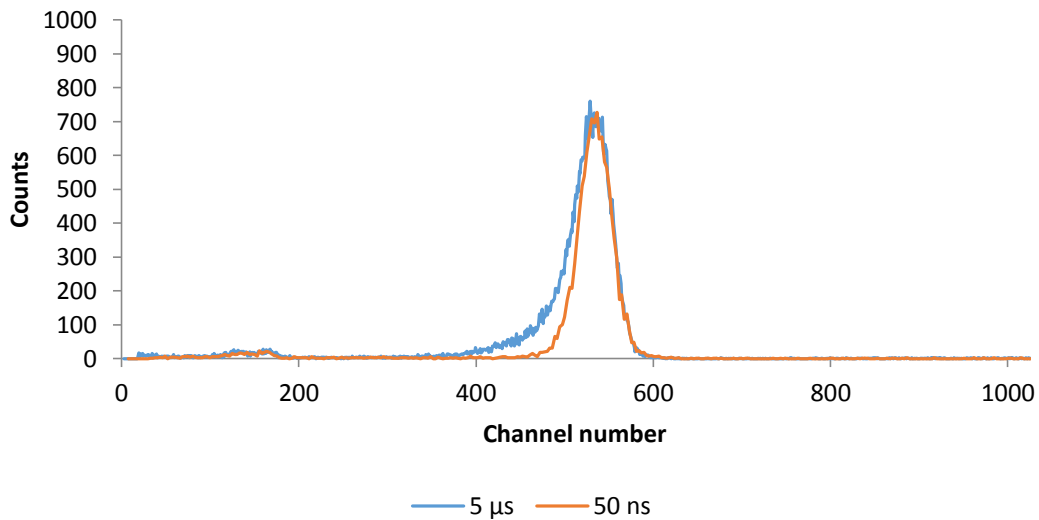
Figure 4.15: Pulse-height distribution of pure xenon with a filling pressure of 804 torr at 100°C, E/p of 4.4 V/cm/torr, a V$_{PMT}$ of 650 V and for shaping constants of 5us and 50 ns.

Figure 4.13 shows that the energy resolution is a little better for 5 μs than for 50 ns (8.38% for 50 ns and 8.04% for 5 μs as shaping constant) as in the studies presented above.

Table 4.2: Excitation threshold for pure xenon for the different operating temperatures of the getters.

Run nº.	xenon pressure (torr)	T$_{getters}$ (°C)	E/p scint (V/cm/torr)
1	1008	195	1.1
2	798	150	1.1
3	810	120	1.1
4	804	100	1.0

Table 4.2 presents the xenon excitation threshold for the studies referred. It is around 1.0 V/cm/torr for the temperature range of 100 – 200°C and it shows that the gas purity achieved, even at a lower temperature, is good enough to not have impact on the gas scintillation threshold.

4.2.2 Electron drift velocity

Total time and fall time were measured for samples of 1000 pulses. Fall time was considered from 95% to 5% of the maximum pulse amplitude. The digital oscilloscope put these values in two histograms and the mode of the histograms was used to calculate the electron drift velocity. To estimate the drift velocity of electrons, the ^{55}Fe source was used.
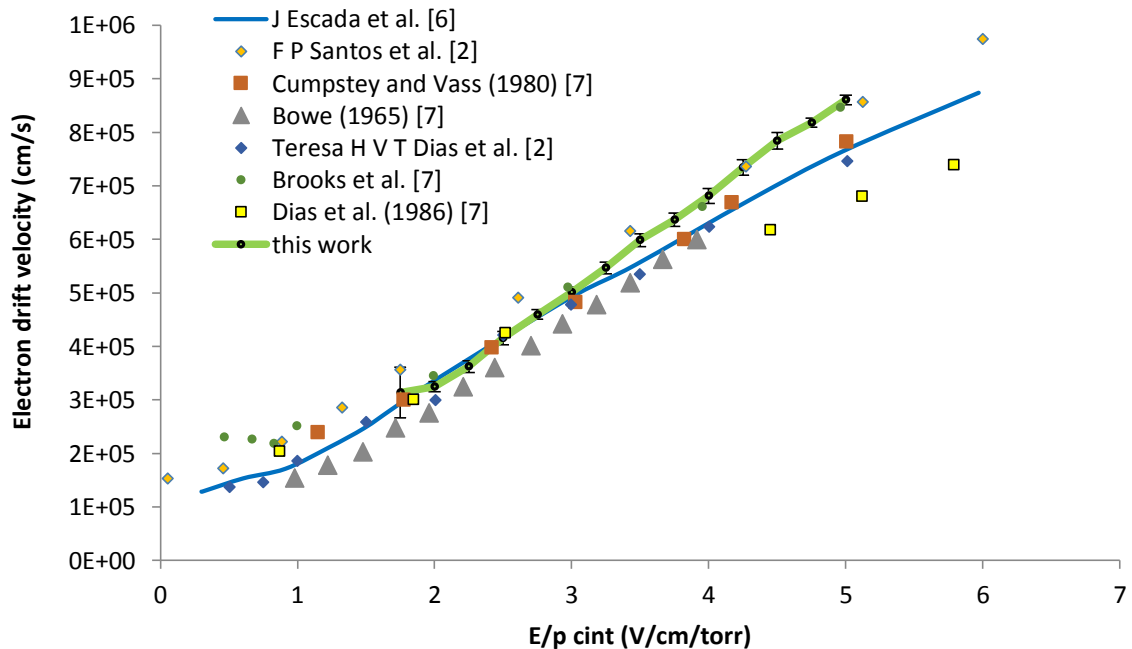
Figure 4.16: Comparison of electron drift velocity for pure xenon as a function of scintillation E/p for our experimental work and for different experimental results and theoretical simulations of Escada et al. [6] and references therein [2,7].

The experimental results of this work are in good agreement with Monte Carlo Simulations and experimental results of other authors of Escada et al. [6] and references therein [2,7].

4.3 Mixtures of xenon and CH$_4$

In this section we report results of mixtures of xenon with 0.5%, 1% and 2% of CH4. A comparison is made with the results for pure xenon.

4.3.1 (99.5% Xe + 0.5 % CH$_4$)

Figure 4.17 shows the variation of the linear dependence of the amplitude on the reduced electric field with time, beginning when 0.5% of CH4 was added to the xenon. The excitation threshold decreases from 1.76 V/cm/torr at for 2.5 hours after adding the CH4, to 1.46V/cm/torr at for 118 hours after adding the CH4, approximating from approaching the xenon excitation threshold, because getters were purifying xenon the filling gas by catching absorbing the methane. This behavior shows that, when using mixtures that include CH$_4$, the detector cannot be operated with the getters at 150°C, because the mixture will not be stable.
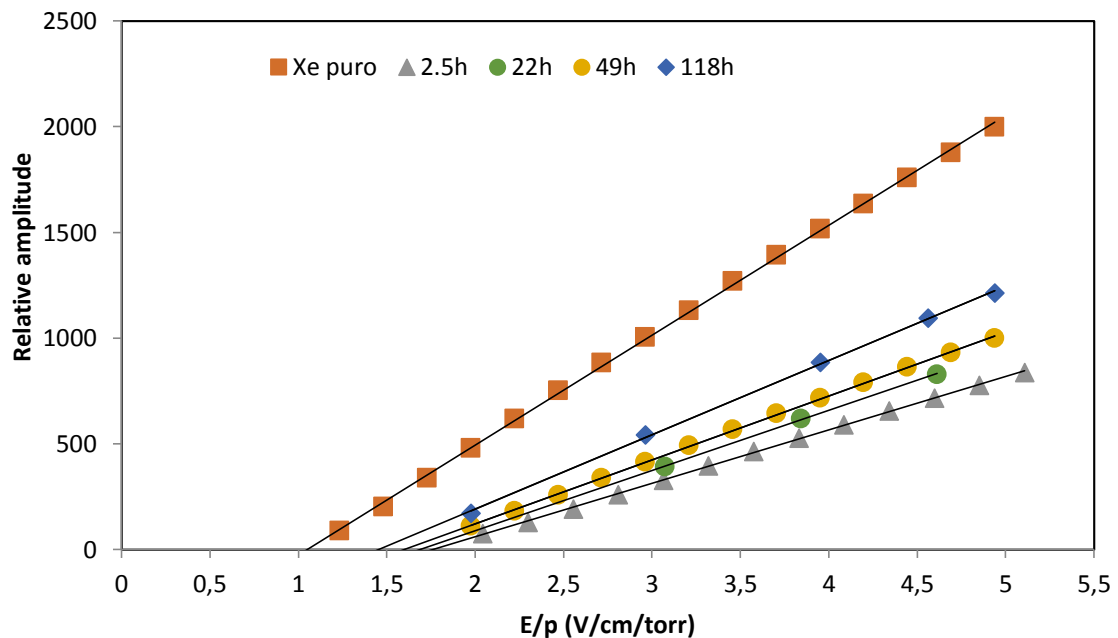
Figure 4.17: Relative amplitude and energy resolution as a function of reduced electric field, E/p, for the mixture of 99.5% of Xe and 0.5% of CH_4 at 150°C with a filling pressure of 790 torr, for a constant PMT bias voltage of 800 V and a shaping constant of 5 μs.
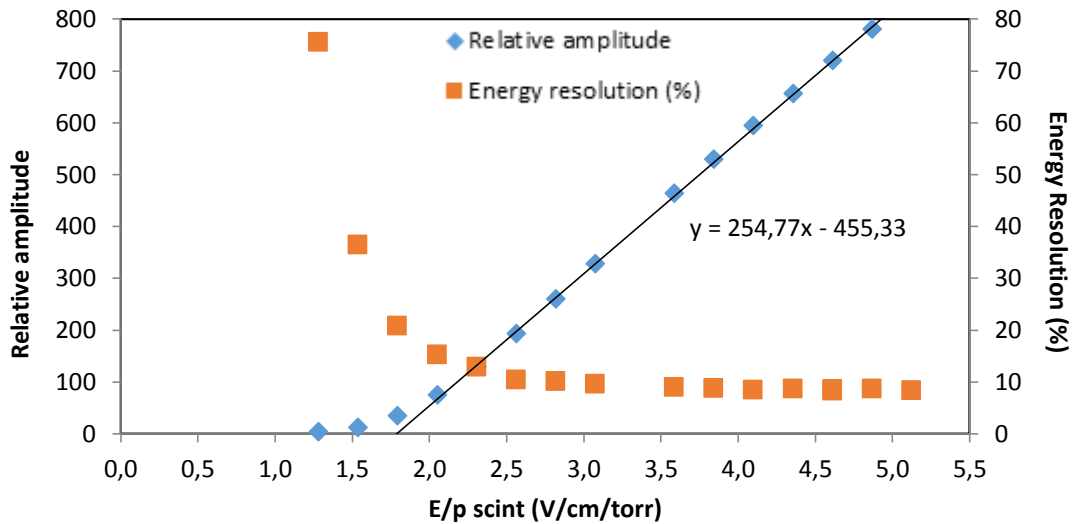

Figure 4.18: Relative amplitude and energy resolution as a function of reduced electric field, E/p, for the mixture of 99.47% Xe and 0.53% CH_4 at 150°C with a filled pressure of 791 torr, with a constant PMT bias voltage of 650 V and formatting constant of 5 μs, 2.5 hour after adding methane to the xenon.

For the mixture (99.47% Xe + 0.53% CH4), the excitation threshold is 1.8 V/cm/torr, higher than pure xenon excitation threshold, as expected. This means that a small percentage of methane added to xenon in the driftless GPSC decreases EL and so it is needed a high electric field to excite xenon atoms (see figure 4.18).

Figure 4.19 shows electron drift velocity from Escada et al. [6] and for the experimental results of this work, for the (99.5% of Xe + 0.5% of CH_4) mixture.
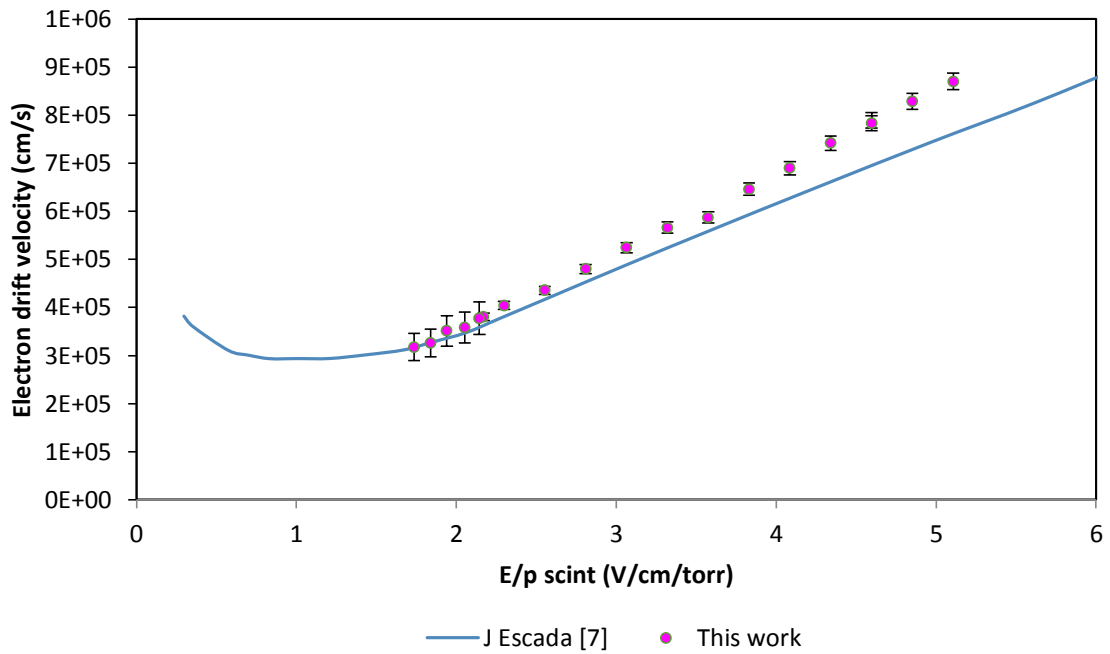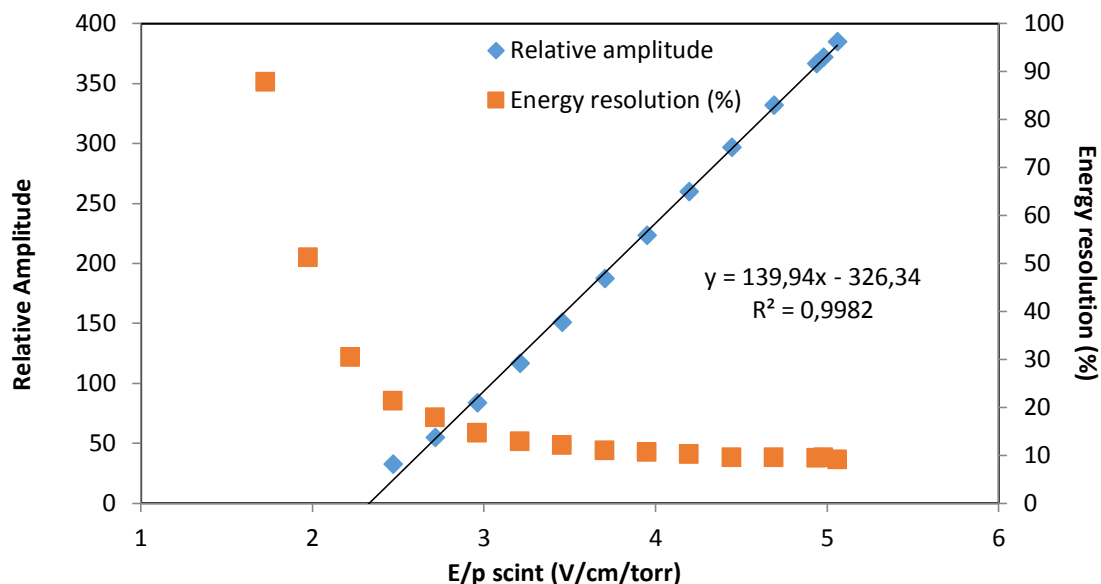
Figure 4.19: Comparison of electron drift velocity from Escada simulations [6] and experimental results of this work for the mixture (99.5% of Xe and 0.5% of CH4)

Experimental results from this work approach from the Monte Carlo simulations, mainly for smaller E/p values.
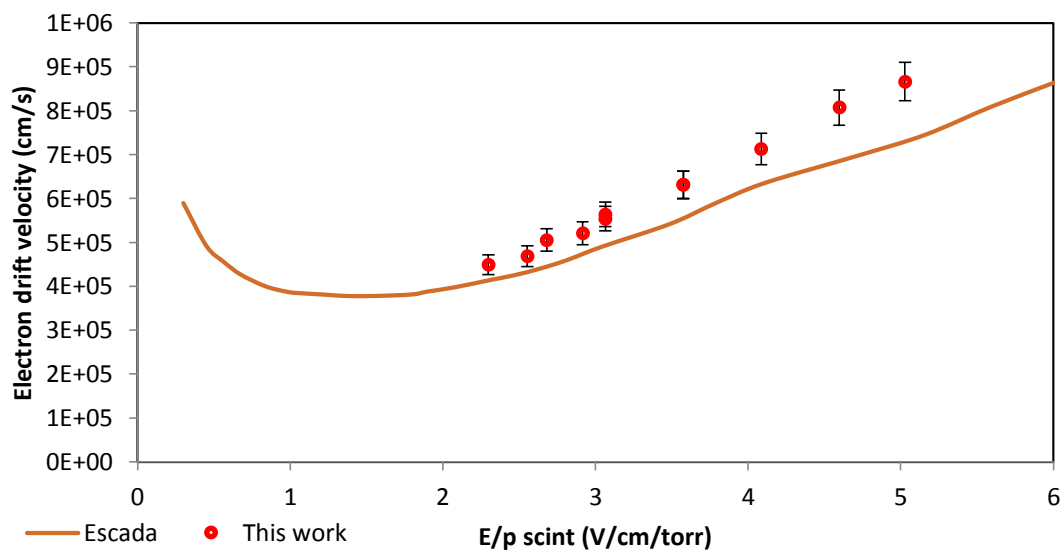
4.3.2   (99% Xe + 1 % CH$_4$)

Figure 4.20 shows amplitude and energy resolution as a function of reduced electric field for the mixture of (99% of Xe and 1% of CH$_4$) with a gas pressure of 790 torr, for a PMT bias voltage of 800 V and long shaping constant, 5 µs.

As shown in figure 4.20, for this mixture (99% of Xe and 1% of CH$_4$), the excitation threshold is 2.33 V/cm/torr, and it is higher than the one for pure xenon and also higher than the one for the mixture (99.5% Xe + 0.5 % CH$_4$), as expected.

Figure 4.20: Amplitude and energy resolution as function of reduced electric field, E/p for the mixture of 99% of Xe and 1% of CH_4 at 100°C with a filled pressure of 790 torr, with a constant PMT bias voltage of 800 V and formatting constant of 5 µs

For the mixture (99 % Xe + 1 % CH_4), the excitation threshold is 2.33 V/cm/torr (see figure 4.21), higher than pure xenon and xenon with 0.5% of CH_4 excitation thresholds, as expected.

Figure 4.21: Comparison of electron drift velocity from Escada simulations [6] and experimental results of this work for the mixture (99% of Xe and 1% of CH4)

The results of electron drift velocity, for xenon with 1% of CH_4, are in good agreement with those obtained in Monte Carlo simulation (see figure 4.21).

4.3.3   (97.8% Xe + 2.2 % CH_4)
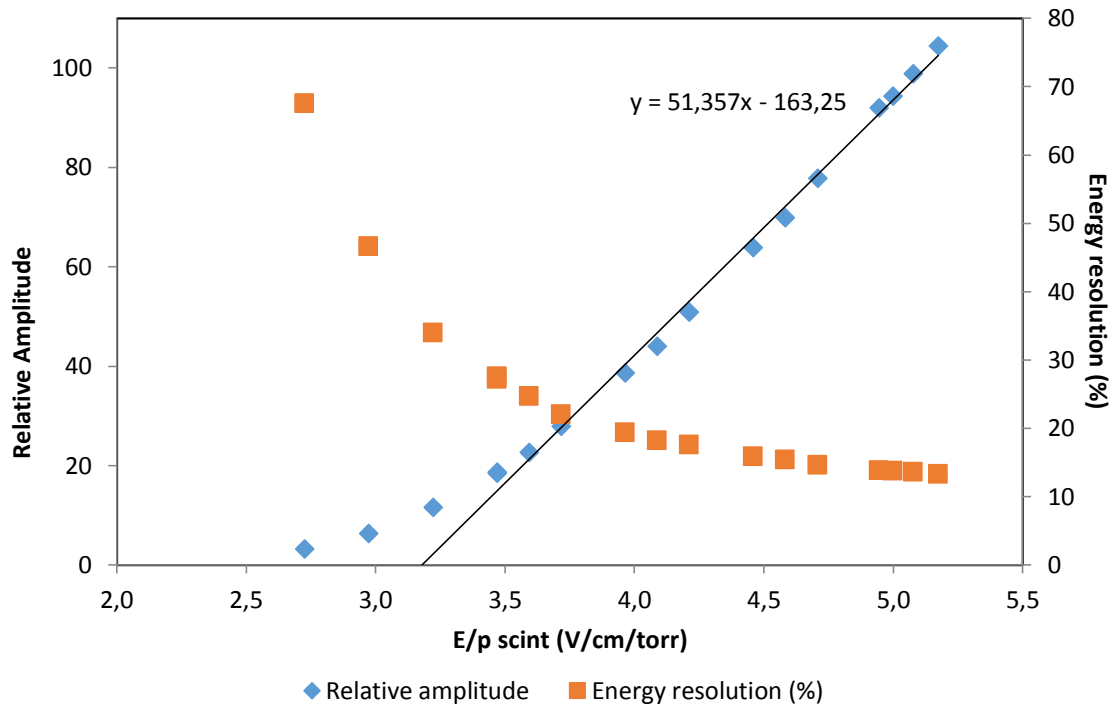
Figure 4.22: Amplitude and energy resolution as function of reduced electric field, E/p for the mixture of 97.8% of Xe and 2.2% of CH_4 at 101.6°C with a filled pressure of 773 torr, with a constant PMT bias voltage of 800 V and formatting constant of 5 µs

For the mixture (97.8 % Xe + 2.2% CH4), the excitation threshold is 3.18 V/cm/torr, (see figure 4.22). Energy resolution stabilizes for E/p close to 5 V/cm/torr with 13%.

Figure 4.23 shows electron drift velocity from Escada et al. [6] and experimental results of this work for (97.8% of Xe and 2.2% of CH4) mixture.
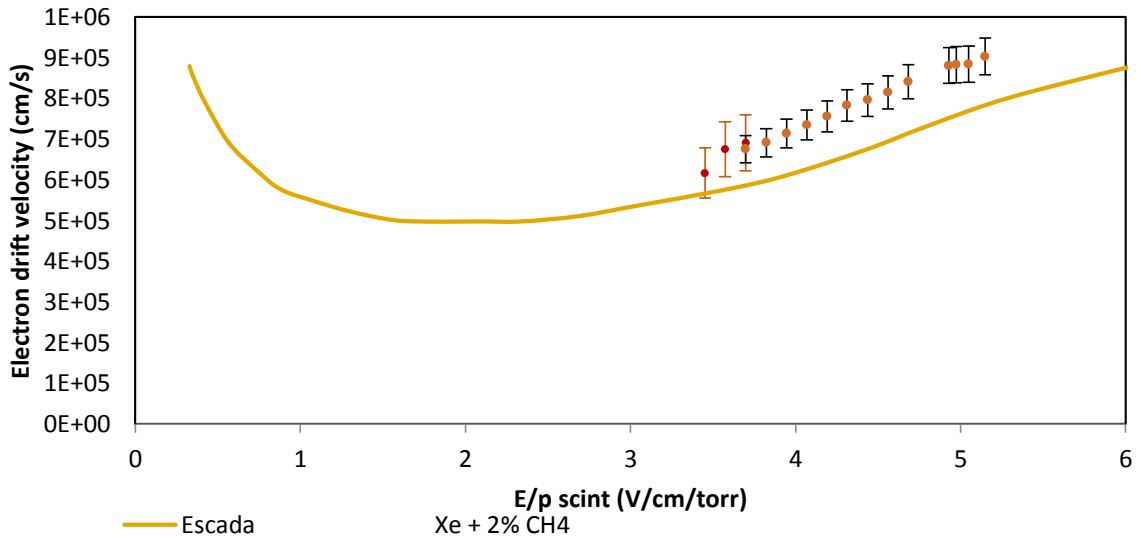
Figure 4.23: Comparison of electron drift velocity from Escada simulations [6] and experimental results of this work for the mixture (98% of Xe and 2% of CH4)

The results for the electron drift velocity of xenon with 2.2 % of CH_4 are in good agreement with those obtained in Monte Carlo simulation for 2% of CH_4, as seen in figure 4.23.

4.3.4   Longitudinal diffusion

We tried to calculate longitudinal diffusion coefficients and energy characteristic, ε_{kL} as a function of the scintillation reduced electric field using equations (2.13) to (2.15), measuring the fall time of the pulse wave as referred in chapter 2. However, the results obtained are not coherent. This is due to the fact that the pre amplifier used was not fast enough, resulting in longer fall times than the correct ones that it would be obtained if we used a faster pre-amplifier.

4.4   Comparison between pure xenon and doped xenon

First we made a comparison of energy resolution as a function of the reduced electric field, for xenon and xenon-methane mixtures. Figure 4.22 presents that comparison.
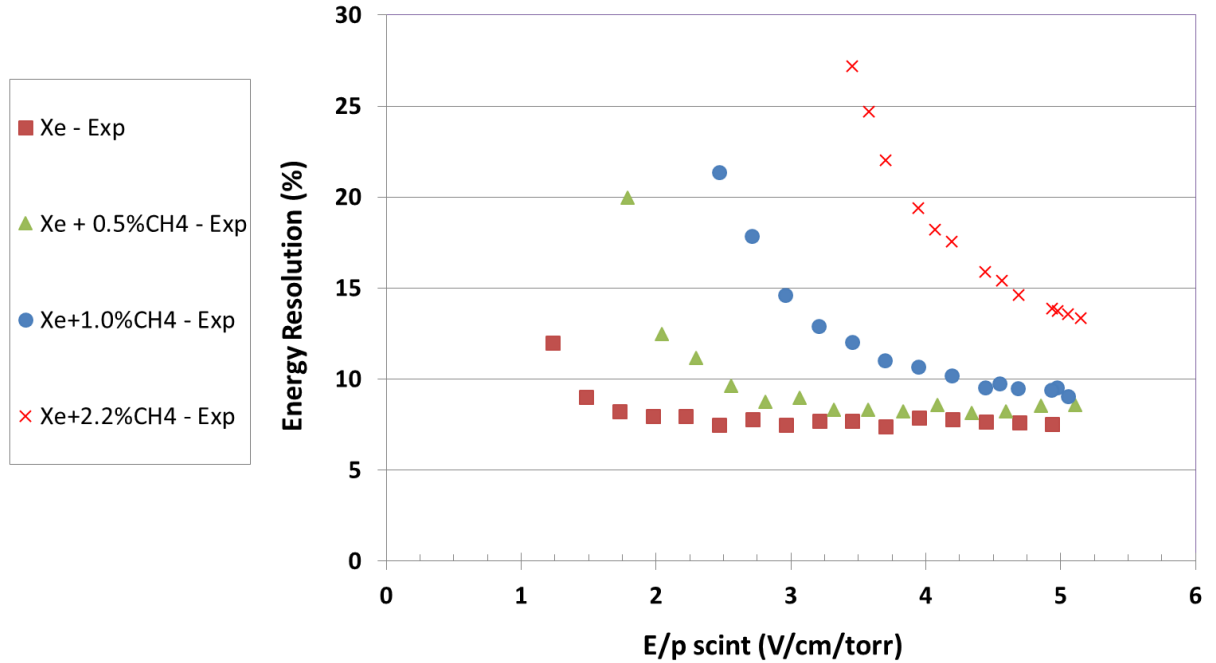
Figure 4.24: Energy resolution as a function of the scintillation reduced electric field, E/p_{scint} for pure xenon and xenon-methane mixtures.

As seen in figure 4.24, higher the percentage of methane added to xenon, higher the energy resolution. For instance, for a E/p of 3.5 V/cm/torr, energy resolution has values of 7.7%, 8.3% and 12% for pure xenon, (99.5% of xenon and 0.5% of CH4), (99% of xenon and 1% of CH4), respectively.

Extrapolating energy resolutions obtained in this work for the E/p conditions of NEXT-TPC but at 1 bar, we obtain the values presented in tables 4.3 and 4.4. We considered E/p values of 3.5 and 4.7 V/cm/torr because NEXT-TPC will operate in this range of scintillation reduced electric field.

At 10 bar, the energy resolution is approximately two times the energy resolution at 1 bar. Therefore, with reduced electric field of 3.5 V/cm/torr, the mixtures (99 %Xe and 1% of CH4) and (98% of Xe and 2% of CH4) are out of the admissible range, i.e. its values are higher than 1 %. For a reduced electric field of 4.7 V/cm/torr, the mixture (98% of Xe and 2% of CH4) is excluded.

Table 4.3: Extrapolation of energy resolution, ER, for 2.5 MeV for an applied E/p of 3 V/cm/torr at 1 bar and the voltage applied to the drift and scintillation regions of NEX-TPC

E/p (V/cm/torr) =	3.5			0.15
	ER(%) for 5.9 keV	ER(%) for 2458 keV	HV (kV) Scint. region	HV (kV) Drift region
Xe	7,7	0,38		
Xe+0.5%CH$_4$	8,3	0,41	7.98 @ 10 bar 11.97 @ 15 bar	114 @10 bar 171 @15 bar
Xe+1%CH$_4$	12,0	0,59		
Xe+2.2%CH$_4$	27,0	1,32		

Table 4.4: Extrapolation of energy resolution for 2.5 MeV for an applied E/p of 4.7 V/cm/torr at 1 bar and the voltage applied to the drift and scintillation regions of NEX-TPC

E/p (V/cm/torr) =	4.7			0.15
	ER (%) for 5.9 keV	ER(%) for 2458 keV	HV (kV) Scint. region	HV (kV) Drift region
Xe	7,61	0,37		
Xe+0.5%CH$_4$	8,45	0,41	10.72 @10bar 16.07 @15bar	114 @10 bar 171 @15 bar
Xe+1%CH$_4$	9,5	0,47		
Xe+2.2%CH$_4$	14,6	0,72		

In this section it is also compared Monte Carlo simulations with experimental results for pure xenon and doped xenon. It is also compared electron drift velocity for the different mixtures, longitudinal diffusion coefficients and characteristic energy related to longitudinal diffusion, as function of E/p for those mixtures.
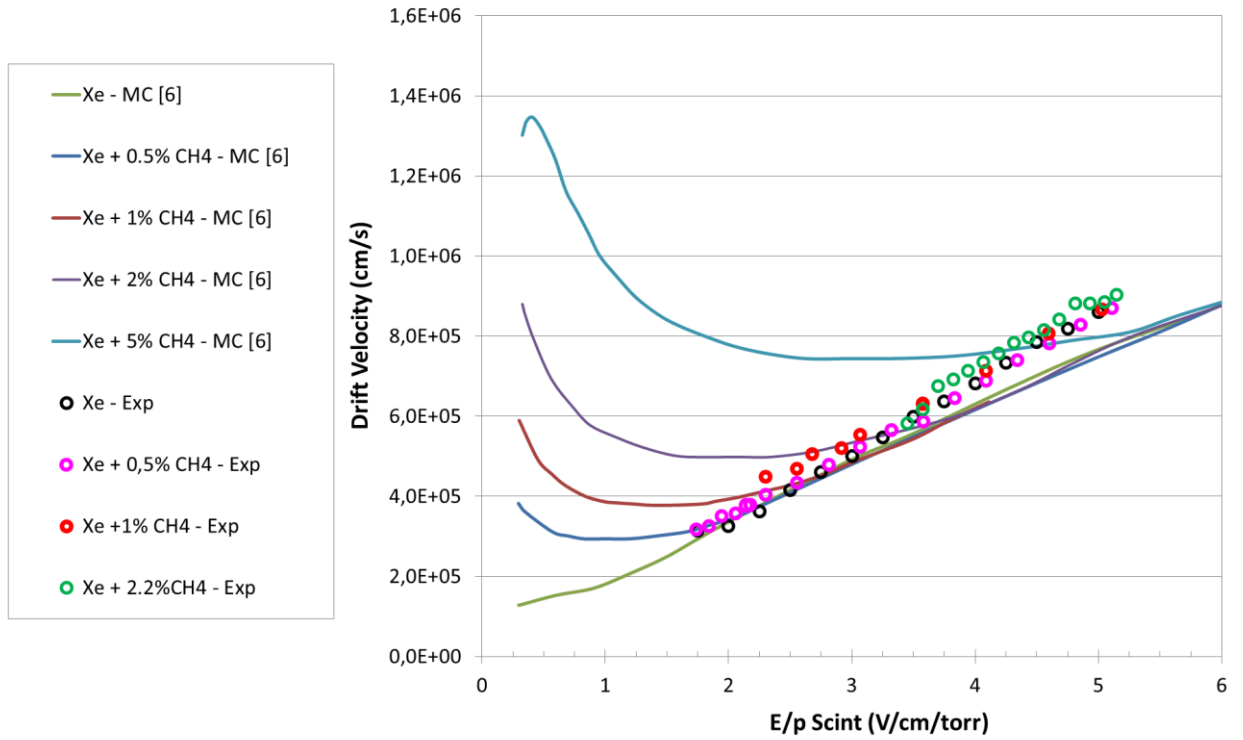
Figure 4.25: Comparison of electron drift velocity as function of E/p for Monte Carlo simulations (lines) [6] and our experimental results (symbols)

In figure 4.25 are present all of our electron drift results which are compared with Monte Carlo simulations. Most of them are in good agreement with those obtained with simulations.

4.5 Electroluminescence yield

In this section, we calculated the reduced EL yield for different values of the reduced electric field, for (Xe+CH$_4$) mixtures.

Figure 4.26 presents the reduced EL yield, Y/N, i.e. the EL yield divided by the density of the gas, as a function of reduced electric field, E/P, in the scintillation region of the driftless GPSC. Experimental results from other authors and results from Monte Carlo simulation [6] are included for comparison.

The results obtained in this work were relative amplitudes. Absolute values were obtained normalizing the relative values of pure xenon to the absolute values C. M .B. Monteiro et al. [9] for pure xenon.
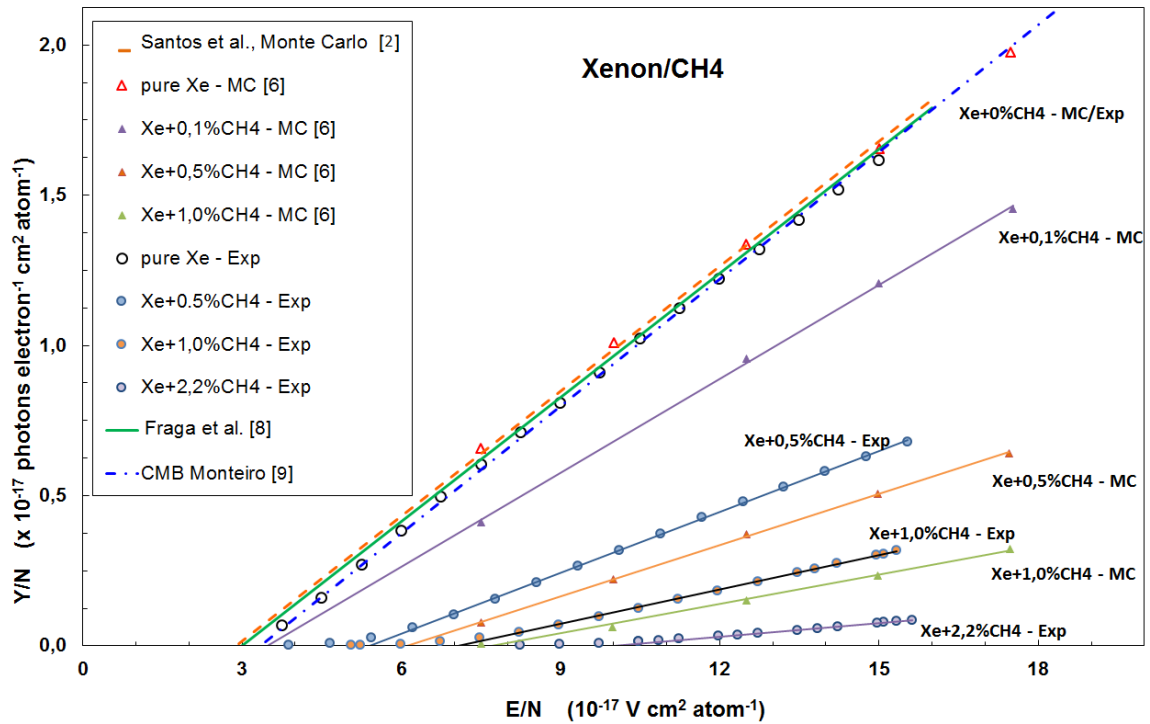
Figure 4.26: Xenon reduced electroluminescence yield as a function of reduced electric field for our studies, as well as for the different data reported in the literature.

Tables 4.3 and 4.4 present the dependencies between Y/N and E/N or E/p for the mixtures (99.5% Xe and 0.5% CH$_4$) and (99% Xe and 1% CH$_4$), respectively, and from Monte Carlo simulation results for the same mixtures.

Table 4.5: Scintillation amplification parameter for the mixture (99.5% Xe and 0.5% CH4), reduced electroluminescence yield linear trends at 20°C for the present studies, as well as for Monte Carlo simulation results [6].

Work	Amplification parameter (photon/kV)	Linear Trend Density units*
Our work	68	Y/N = 0.068 E/N- 0.366
MC Escada	57	Y/N = 0,057E/N − 0.348

* *E/N* in Td (10^{-17} V cm^2 atom^{-1})

Table 4.6: Scintillation amplification parameter for the mixture (99% Xe and 1% CH4), reduced electroluminescence yield linear trends at 20°C for the present studies, as well as for Monte Carlo simulation results [6].

Work	Amplification parameter (photon/kV)	Linear Trend Density units*
Our work	38	Y/N = 0.038 E/N – 0.269
MC Escada	32	Y/N = 0.032 E/N – 0.248

* E/N in Td (10^{-17} V cm^2 atom^{-1})

For the mixture of 97.8% xenon and 2.2% CH$_4$, the variation of the reduced electroluminescence yield with reduced electric field in temperature independent units can be approximately represented by

$$Y/N \ (10^{-17} photons \ electron^{-1} cm^2 atom^{-1} = \ 0.0149 \frac{E}{N} - \ 0.1479 \qquad 4.1$$

where E/N is given in Td (10^{-17} V cm^2 atom^{-1}).

And the amplification parameter for the mixture (97.8% Xe and 2.2% CH$_4$) is 14.9 photons/kV.

As shown, the amplification parameters for the mixtures (99.5% Xe and 0.5% CH4) and (99% Xe and 1% CH4) are not very different from those predicted by Monte Carlo simulation for the same mixtures. Compared to pure xenon, the EL yield decreases to 50% for 0.5% of CH$_4$, to 30% for 1% of CH$_4$ and to 10% for 2.2% of CH$_4$. This proves that the amount of secondary scintillation in noble gases decreases with increasing impurity content.

4.6 References

[1] L.M.P. Fernandes, E.D.C. Freitas, M. Ball, et al., *Primary and secondary scintillation measurements in a xenon Gas Proportional Scintillation Counter*, JINST 5 (2010) P09006 doi:10.1088/1748-0221/5/09/P09006

[2] F P Santos, T H V Dias, A D Stauffer and C A N Conde, T*hree − dimensional Monte Carlo calculation of the VUV electroluminescence and other electron transport parameters in xenon*, J. Phys. D: Appl. Phys. 27 (1994) 42

[3] D.G. Simons and P.A.J. De Korte, *Soft X-ray energy resolution and background rejection in driftless gas scintillation counter*, Nucl. Instr. And Meth. A277 (1989) 642

[4] P.C.P.S. Simões, D.S. Covita, J.F.C.A. Veloso, *A new method for pulse analysis of driftless-gas proportional scintillation counters*, Nuclear Instruments and Methods in Physics Research A 505 (2003) 247

[5] D.S. Covita, P.C.P.S. Simões, L.M.P. Fernandes, *The X-ray performance of a driftless gas proportional scintillation counter using short shaping-time constants for pulse analysis*, Nuclear Instruments and Methods in Physics Research A 516 (2004) 134

[6] J. Escada, T.H.V.T. Dias, F.P. Santos et al, A Monte Carlo study of the fluctuations in Xe electroluminescence yield: pure Xe vs Xe doped with CH4 or CF4 and planar vs cylindrical geometries, JINST 6 (2011) P08006

[7] Teresa H V T Dias, A D Stauffer and C A N Conde, *A unidimensional Monte Carlo simulationo f electron drift velocities and electroluminescence in argon, krypton and xenon*, J. Phys. D: Appl. Phys1. 9 (1986) 527

[8] M M F R Fraga, C M Ferreira, J Loureiro and MS Leite, P 1990 ESCAMPIG (Orleans, France, 28-31 Aug)

[9] C. M .B. Monteiro, L. M. P. Fernandes, J. A. M. Lopes, et al., *Secondary scintillation yield in pure xenon*, JINST 2 (2007) P05001

5. Conclusion

Since the early development of GPSCs with uniform field geometries, the approximately linear dependence of the reduced EL yield on the reduced electric field in the scintillation region is well stablished and known. The scintillation threshold corresponds to a reduced electric field of about 0.8 kV/cm/bar (or 1.0 V/cm/torr) [1] for pure xenon.

However, for xenon-CH_4 mixtures, the amplification parameter (the number of photons produced per drifting electron and per volt – the slope of the linear dependence referred to above) has not been well established in the literature yet, presenting only values from one Monte Carlo simulation model [2]. In the experimental work described in this thesis, this parameter was measured and was found to decrease for these mixtures and, the higher the percentage of the impurity, the smaller the amplification parameter, in agreement with the Monte Carlo results.

A scintillation amplification parameter of pure xenon were used as reference to obtain the relative EL yields of 68 photons/kV for xenon with 0.5% of CH_4, 38 photons/kV for 1% of CH_4 and 15 photons/kV for 2.2% of CH_4. This compares with the Monte Carlo values of 57 and 32 photons/kV for Xe+0.5% CH_4 and Xe+1.0% CH_4, respectively. This reduction in EL has to be taken into account if the addition of CH_4 to xenon is to be considered. A compromise between the mixture EL yield and electron diffusion has to be found, depending on the application.

Comparing with Monte Carlo simulations results of the EL yield, we had more 19% of EL in this work than in simulations made by Escada et al. [2]. We know that these simulations considered ideal conditions and did not take account all the effects that happen in the detector.

The results of electron drift velocity for pure xenon and mixtures are in good agreement with those obtained with Monte Carlo simulations, as shown in figure 4.25.

For the NEXT experiment, the energy resolution parameter is more important than the EL yield, which can be more than what is needed for optimum energy resolution. The energy resolution in NEXT should be as close to the intrinsic value as possible, i.e. the lowest achievable for a GPSC. Our studies have shown that the (99.5 % Xe and 0.5% CH4), (99.0 % Xe and 1.0% CH4) mixtures are adequate for using in NEXT, since the energy resolution is inferior to 1%. However, longitudinal diffusion must be calculated and analysed to decide the best choice for the NEXT TPC.

5.1 Future Work

The next work is studying the attachment in deep drift region, the electron diffusion and calculate the w-value of the mixtures of Xe-CH$_4$. The similar studies should be extended to mixtures of xenon with the addition of other molecular gases, namely H$_2$ and trimethylamine (TMA), as we already know that CF$_4$ additive, as well as N$_2$ worsens the TPC performance. CF$_4$ presents strong attachment of primary electrons and for N$_2$ has been shown experimentally that degrades the energy resolution. TMA, added to xenon, may permit a large TPC to be operated with better than the intrinsic energy resolution of pure xenon. This path is being explored within the NEXT collaboration. TMA may provide a strong Penning effect and also permit electroluminescence at wavelengths characteristic of TMA [3, 4, 5]. However, it is yet to be proven that TMA does not absorb the xenon primary and secondary scintillation.

5.2 References

[1] M.A. Feio, A.J.P.L. Policarpo, M.A.F. Alves, Jap. J. Appl. Phys. 8 (1982) 1184.

[2] J. Escada, T.H.V.T. Dias, F.P. Santos et al., A Monte Carlo study of the fluctuations in Xe electroluminescence yield: pure Xe vs Xe doped with CH$_4$ or CF$_4$ and planar vs cylindrical geometries, JINST 6 (2011) P08006

[3] David Nygren, *Can the "intrinsic" energy resolution in xenon be surpassed?*, Journal of Physics: Conference Series 309 (2011) 012006

[4] D C Herrera, S Cebrián, T Dafni1 et al., *Micromegas-TPC operation at high pressure in Xenon-trimethylamine mixtures*, Journal of Physics: Conference Series 460 (2013) 012012

[5] A. Goldschmidt, V. Gehman, M. Long et al., *Development of High Pressure Xenon Detectors for Dark Matter and Neutrino-less Double Beta Decay*, Lawrence Berkeley National Laboratory for the NEXT Collaboration